Mon. Not. R. Astron. Soc. **371,** 221–234 (2006) doi:10.1111/j.1365-2966.2006.10634.x

A deep *Chandra* survey of the Groth Strip – II. Optical identification of the X-ray sources

A. Georgakakis,[1]★† K. Nandra,[1] E. S. Laird,[1] S. Gwyn,[2] C. C. Steidel,[3] V. L. Sarajedini,[4] P. Barmby,[5] S. M. Faber,[6] A. L. Coil,[7] M. C. Cooper,[8] M. Davis[8,9] and J. A. Newman[10]‡

[1]*Astrophysics Group, Blackett Laboratory, Imperial College, Prince Consort Rd, London SW7 2BZ*
[2]*Department of Physics and Astronomy, University of Victoria, PO Box 3055, Victoria, BC V8W 3P6, Canada*
[3]*California Institute of Technology, Pasadena, CA 91125, USA*
[4]*Department of Astronomy, University of Florida, Gainesville, FL 32611, USA*
[5]*Harvard-Smithsonian Center for Astrophysics, 60 Garden Street, Mail Stop 65, Cambridge, MA 02138, USA*
[6]*UCO/Lick Observatory and Department of Astronomy and Astrophysics, University of California, Santa Cruz, CA 95064, USA*
[7]*Steward Observatory, University of Arizona, 933 N. Cherry Ave., Tucson, AZ 85721-0065, USA*
[8]*Department of Astronomy, University of California, Berkeley, CA 94720, USA*
[9]*Department of Physics, University of California, Berkeley, CA 94720, USA*
[10]*Institute for Nuclear and Particle Astrophysics, Lawrence Berkeley National Laboratory, Berkeley, CA 94720, USA*

Accepted 2006 May 25. Received 2006 May 18; in original form 2005 November 7

ABSTRACT

In this paper, we discuss the optical and X-ray spectral properties of the sources detected in a single 200-ks *Chandra* pointing in the Groth-Westphal Strip region. A wealth of optical photometric and spectroscopic data are available in this field providing optical identifications and redshift determinations for the X-ray population. The optical photometry and spectroscopy used here are primarily from the Deep Extragalactic Evolutionary Probe 2 (DEEP2) survey with additional redshifts obtained from the literature. These are complemented with the deeper ($r \approx 26$ mag) multiwaveband data (*ugriz*) from the Canada–France–Hawaii Telescope Legacy Survey to estimate photometric redshifts and to optically identify sources fainter than the DEEP2 magnitude limit ($R_{\rm AB} \approx 24.5$ mag). We focus our study on the 2–10 keV selected sample comprising 97 sources to the limit $\approx 8 \times 10^{-16}$ erg s^{-1} cm^{-2}, this being the most complete in terms of optical identification rate (86 per cent) and redshift determination fraction (63 per cent; both spectroscopic and photometric). We first construct the redshift distribution of the sample which shows a peak at $z \approx 1$. This is in broad agreement with models where less luminous active galactic nuclei (AGNs) evolve out to $z \approx 1$ with powerful quasi-stellar objects (QSOs) peaking at higher redshift, $z \approx 2$. Evolution similar to that of broad-line QSOs applied to the entire AGN population (both types I and II) does not fit the data. We also explore the *observed* $N_{\rm H}$ distribution of the sample and estimate a fraction of obscured AGN ($N_{\rm H} > 10^{22}$ cm^{-2}) of 48 ± 9 per cent. This is found to be consistent with both a luminosity-dependent *intrinsic* $N_{\rm H}$ distribution, where less luminous systems comprise a higher fraction of type II AGNs and models with a fixed ratio 2:1 between types I and II AGNs. We further compare our results with those obtained in deeper and shallower surveys. We argue that a luminosity-dependent parametrization of the intrinsic $N_{\rm H}$ distribution is required to account for the fraction of obscured AGN observed in different samples over a wide range of fluxes.

Key words: surveys – galaxies: active – cosmology: observations – X-rays: diffuse background – X-rays: galaxies.

1 INTRODUCTION

In the last few years the study of the diffuse X-ray background (XRB) has witnessed significant observational progress allowing detailed comparison with model predictions. The ultradeep *Chandra*

★E-mail: a.georgakakis@imperial.ac.uk
†Marie Curie fellow.
‡Hubble fellow.

surveys, in particular, have demonstrated that most of the XRB, at both soft and hard energies, is resolved into discrete point sources (Brandt et al. 2001; Giacconi et al. 2002; Alexander et al. 2003), the vast majority of which are without doubt active galactic nuclei (AGNs). To the first approximation, this finding has been a huge success for models that reproduce the spectral properties of the XRB under the zero order assumption that it originates in a combination of obscured and unobscured AGN (Comastri et al. 1995; Gilli, Salvati & Hasinger 2001). Under more careful examination, however, a number of inconsistencies emerge. First, luminous ($L_{\rm X} > 10^{44}\,{\rm erg\,s^{-1}}$) heavily obscured type II quasi-stellar objects (QSOs) at $z \approx 1.5$–2, predicted in large numbers by the models, are scarce in the surveys above. Secondly, the redshift peak of the X-ray population lies below $z = 1$ in stark contrast with the model expectation of $z \approx 1.5$–2.

Although these inconsistencies suggest that some revision of the models is almost certainly required (Hasinger 2003), observational biases may complicate any interpretation. For example, about ≈25 per cent of the sources in the *Chandra* Deep Fields (CDF) are optically faint, $R > 24$ mag, rendering optical spectroscopy difficult or even impossible with current technology (Rosati et al. 2002; Barger et al. 2003). Any information about the nature of these sources is therefore limited and they are proposed as best candidates for heavily obscured AGN (Alexander et al. 2001; Treister et al. 2004), likely to comprise a fraction the elusive population of high-z type II QSOs. Moreover, the small field of view of the CDFs ($0.07\,{\rm deg^2}$ each) makes them sensitive to cosmic variance further complicating interpretation of the derived redshift distribution.

Wide-area shallower ($\approx 10^{-14}\,{\rm erg\,s^{-1}\,cm^{-2}}$) surveys are less affected by the observational biases above (e.g. Baldi et al. 2002; Georgantopoulos et al. 2004; Kim et al. 2004). These samples although of key importance, comprise a large fraction of unobscured AGNs that are not representative of the sources responsible for the spectral shape of the XRB ($\Gamma = 1.4$; e.g. Gruber et al. 1999).

The evidence above suggests that deep surveys with relatively wide field of view are essential to improve our understanding of the XRB. Observational programs in this direction are already well underway such as the *XMM–Newton* Cosmic Evolution Survey [COSMOS; $2\,{\rm deg^2}$, $f_{\rm X}(0.5\text{–}2\,{\rm keV}) \approx 5 \times 10^{-16}\,{\rm erg\,s^{-1}\,cm^{-2}}$] and the Extended *Chandra* Deep Field South [E-CDF-S; Lehmer et al. 2005; Virani, Treister & Urry 2006; $0.3\,{\rm deg^2}$, $f_{\rm X}(0.5\text{–}2\,{\rm keV}) \approx 1.1 \times 10^{-16}\,{\rm erg\,s^{-1}\,cm^{-2}}$]. In this paper, we present results on a single 200-ks *Chandra* pointing, which is part of an on-going X-ray survey in the Extended Groth Strip (EGS) region, which will eventually cover a total area of about $0.5\,{\rm deg^2}$ to the depth above (200 ks per pointing). This sample, when completed, will be intermediate in terms of area coverage and depth to the CDFs and shallower wide-area surveys, minimizing any observational biases affecting the ultradeep fields and comprising a large fraction of obscured AGNs responsible of the XRB properties (Nandra et al. 2005). Moreover, the EGS is targeted by the largest space and ground-based facilities for multiwavelength observations: (i) the Deep Extragalactic Evolutionary Probe (DEEP) and DEEP2 surveys provide optical spectroscopy to the limit $R_{\rm AB} \approx 24$ mag, (ii) multiwaveband optical photometry to fainter magnitudes is underway as part of the Canada–France–Hawaii Telescope Legacy Survey (CFHTLS), (iii) deep imaging and spectroscopy, independent from the programs above, has been performed by Steidel et al. (2003) in search for Lyman Break galaxies, (iv) comprehensive imaging with *Hubble Space Telescope* (*HST*)/Advanced Camera for Surveys (ACS) has recently been completed, (v) *Spitzer* mid-infrared (IR) data are available, (vi) radio observations to sub-mJy levels have been obtained by Fomalont et al. (1991) with new much wider Very Large Array (VLA) observations recently completed, (vii) Submillimetre Common-User Bolometer Array (SCUBA) has observed part of this field to the deep limits of the Canada–UK Deep Submillimetre survey (Webb et al. 2003). A combination of the X-ray observations with the mutliwavelength data sets above promises a breakthrough in the study of the evolution and large-scale structure of AGNs as well as the connection between AGN activity and host galaxy formation.

This paper presents the optical and X-ray spectral properties of the sources detected in the first 200-ks *Chandra* pointing observed as part of the EGS X-ray survey. This observation encompasses the original Groth-Westphal Strip (GWS) region (Groth et al. 1994). In addition to studying the properties of the X-ray sources in the context of XRB models, our purpose is to demonstrate the power of the full $0.5\,{\rm deg^2}$ EGS *Chandra* survey, when completed, for XRB studies. Throughout this paper, we adopt $H_0 = 70\,{\rm km\,s^{-1}\,Mpc^{-1}}$, $\Omega_{\rm m} = 0.3$ and $\Omega_\Lambda = 0.7$.

2 DATA

2.1 X-ray observations

The X-ray data used in this paper are from the A03 *Chandra* observations of the original GWS, which is part of the EGS region. The total exposure time is about 190 ks split into three separate integrations obtained at different epochs. All three observations were obtained with the ACIS-I instrument ($17 \times 17\,{\rm arcmin^2}$) with a similar roll angle at the aim point, $\alpha = 14{:}17{:}43.6$, $\delta = 52{:}28{:}41.2$. A detailed description of the data reduction, source detection and flux estimation has been presented by Nandra et al. (2005).

Briefly, standard reduction methods were applied using the CIAO version 3.0.1 data analysis software. After merging the individual observations into a single event file, we constructed images in four energy bands 0.5–7.0 keV (full), 0.5–2.0 keV (soft), 2.0–7.0 keV (hard) and 4.0–7.0 keV (ultrahard). Source detection was performed using a simple but efficient method which is based on pre-selection of candidate sources using the WAVDETECT task of CIAO followed by aperture count extraction using the 90 per cent point spread function (PSF) radius and a local background determination to estimate the source significance. The final catalogue used in this paper comprises a total of 158 sources over a total surveyed area of $0.082\,{\rm deg^2}$ to a Poisson detection probability threshold $< 4 \times 10^{-6}$. Of these sources a total of 155, 121, 97 and 44 are detected in the full, soft, hard and ultrahard bands, respectively. Fluxes are estimated by integrating the net counts within an aperture corresponding to the 70 per cent encircled energy radius at the position of the source. The counts in the full, soft, hard and ultrahard bands are converted into fluxes in standard bands, 0.5–10, 0.5–2, 2–10 and 5–10 keV, respectively. The limiting flux in each of these bands is estimated 3.5×10^{-15}, 1.1×10^{-16}, 8.2×10^{-16} and $1.4 \times 10^{-15}\,{\rm erg\,s^{-1}\,cm^{-2}}$, respectively.

2.2 Optical photometry

The main photometric catalogue used in this paper for the optical identification of the X-ray sources is the DEEP2 survey of the EGS that also overlaps with the original GWS field.

The DEEP2 survey photometric data were obtained at the Canada–France–Hawaii Telescope (CFHT) using the 12×8 k pixel CCD mosaic camera providing a $0.70 \times 0.47\,{\rm deg^2}$ field of view per pointing. The observations were performed in the *B*, *R* and *I*

filters. The data reduction, source detection, photometric and astrometric calibration as well as the star–galaxy separation are described in Coil et al. (2004). The pointing that overlaps with the *Chandra* X-ray data used here is nearly complete to $R_{\rm AB} \approx 24.50$ mag ($B_{\rm AB} \approx 24.75$ mag, $I_{\rm AB} \approx 23.5$ mag). This is shallower than the nominal limit of the full DEEP2 EGS survey ($R_{\rm AB} \approx 24.75$ mag) because of poorer seeing conditions (about 0.95 arcsec) at the time of the observations (Coil et al. 2004). The astrometric accuracy of the photometric catalogue is estimated to be 0.5 arcsec and is limited by systematic errors of the USNO-A catalogue used to determine the astrometric solution.

The GWS also overlaps with the ongoing deep synoptic CFHTLS. This project uses the wide field imager MegaPrime equipped with the MegaCam CCD array providing a $1 \times 1\,{\rm deg}^2$ field of view. In this paper, we use the first data obtained as part of the deep synoptic survey in the *ugriz* filters. The exposure times in each waveband range from 1 to 13 h (depending on the filter) corresponding to about 2–9 per cent of the target integration at the completion of the project. The data reduction, source detection, photometric and astrometric calibration will be presented in a future paper. In brief, the ELIXIR package was used for the reduction as well as the initial photometric and astrometric calibration, which were then refined using our own routines. The final astrometric uncertainty is estimated to be about 0.3 arcsec. The photometric accuracy is found to be better than 0.05 mag in all filters while the completeness limit in the AB system is $r \approx 26$ mag ($u \approx 25.5$ mag, $g \approx 26.0$ mag, $i \approx 25.5$ mag, $z \approx 25.0$ mag). Although the CFHTLS deep synoptic data set reaches fainter limits that the DEEP2, we prefer to use the latter at present as the basic photometric catalogue because of its homogeneity and the well-documented observational properties of this survey (e.g. Coil et al. 2004; Faber et al. 2005; Willmer et al. 2005). We nevertheless use the multiwaveband photometry of the CFHTLS primarily to estimate photometric redshifts but also to search for X-ray source optical counterparts that are fainter than the DEEP2 limit.

Finally, the GWS has been targeted for deep optical imaging as part of a larger program searching for Lyman Break galaxies (Steidel et al. 2003). The observations were performed at the Kitt Peak 4-m Mayall telescope using the Prime Focus CCD camera ($14.2 \times 14.2\,{\rm deg}^2$ field of view) in the *Un*, *G* and $\Re$ filters. Because of the smaller field of view of these observations the outer edges of X-ray pointing do not overlap with the optical image. A detailed description is presented by Steidel et al. (2003). The astrometry is accurate to about 0.4 arcsec and the photometric internal scatter is estimated to be better than 0.03 mag in all filters. These observations reach a limiting magnitude $\Re_{\rm AB} \approx 26$ mag, similar to the CFHTLS. They are used here primarily to estimate photometric redshifts using the Lyman Break selection criteria. As discussed by Steidel et al. (2003), these methods are very efficient in identifying galaxies in narrow redshift slices in the range $1.5 \lesssim z \lesssim 3$.

We note that the *R*-band filters used in the above three data sets are similar and, therefore, there is good agreement in the estimated *R*-band magnitudes of the same object among the different surveys.

2.3 Optical spectroscopy

The main source of optical spectroscopy in this study is the DEEP2 redshift survey. This is an ongoing project that uses the DEep Imaging Multi-Object Spectrograph (DEIMOS) on the 10-m Keck II telescope aiming to obtain redshifts for about 40 000 galaxies in the range $0.7 \lesssim z \lesssim 1.5$ to a limiting magnitude $R_{\rm AB} = 24.1$ mag. The spectra are obtained with a high resolution grating (1200 line mm^{-1}, $R \approx 5000$) and span the wavelength range 6500–9100 Å. This spectral window allows the identification of the O II emission line in the redshift interval $0.7 \lesssim z \lesssim 1.4$. Outside this range the ability to measure redshifts and hence, the completeness of the DEEP2, drops significantly. The data reduction was performed using an interactive data language (IDL) based pipeline developed at UC-Berkeley (Cooper et al. 2006) and adapted from reduction programs created for the Sloan Digital Sky Survey (SDSS).

The GWS has also been targeted by a number of spectroscopic programs (Lilly et al. 1995; Brinchmann et al. 1998; Hopkins, Connolly & Szalay 2000; Voght et al. 2005) that have been compiled into a single data base by Weiner et al. (2005).[1] The entire EGS overlaps with the SDSS and therefore spectra for relatively bright galaxies and QSOs are also available (York et al. 2000).

In addition to the above surveys Steidel et al. (2003, 2004) performed follow-up multislit spectroscopy of the GWS Lyman Break galaxies as well as some X-ray sources using the blue channel of the Low Resolution and Imaging Spectrograph (LRIS-B) on the Keck telescopes. The observations used a 300 line mm^{-1} grating blazed at 5000 Å leading to a dispersion of 2.47 Å pixel^{-1}, a wavelength range that included at least the 4000–7000 Å regime and a nominal spectral resolution of about 12.5 Å. The total integration time varied between 1.5 and 3 h (depending on the observing conditions), split into 1800 s subexposures followed by a dither of the telescope in the slit direction. The data were reduced using a custom package based on IRAF scripts. A total of 10 sources in our sample have redshift measurements from these observations.

3 OPTICAL IDENTIFICATION

The main catalogue used to optically identify the GWS X-ray sources is the DEEP2 survey. We first search for systematic offsets between the astrometric solutions of the X-ray and optical catalogues. A matching radius of 2 arcsec is adopted to include only secure optical identifications. We also consider X-ray sources with off-axis angles <6 arcmin (total of 86) where the *Chandra* PSF is superior with a 90 per cent encircled energy radius of $\lesssim$4 arcsec. A total of 50 X-ray sources have optical identifications brighter than $R_{\rm AB} < 24.5$ mag. We estimate small systematic offsets of $\delta{\rm RA} = -0.23$ and $\delta{\rm Dec.} = 0.37$ arcsec between the X-ray and optical source positions. These were then used to align the X-ray source catalogue to the DEEP2 astrometric solution.

Next we explore the positional accuracy of the X-ray centroid as a function of off-axis angle, θ. We match the X-ray and optical catalogues using an ample 5-arcsec search radius to account for the degradation of the PSF at large off-axis angles. Fig. 1 plots the positional offset in RA and Dec. between the X-ray and optical source positions against θ. Reassuringly, the mean X-ray-optical offset is close to zero at all off-axis angles but the 1σ rms increases from about 0.5 arcsec at $\theta \lesssim 6$ arcmin to $\approx$1 arcsec at larger off-axis angles. We account for the degradation of the X-ray positional accuracy by varying the matching radius as a function of off-axis angle. For $\theta \leqslant 6$ arcmin, we use a radius of 1.5 arcsec, corresponding to the 3σ rms scatter around the mean. For $\theta > 6$ arcmin the matching radius increases to 3 arcsec, the 3σ rms positional uncertainty at these off-axis angles.

The surface density of optical sources to the limit $R_{\rm AB} = 24.5$ mag is large enough that a substantial fraction of chance associations is expected within the above radii. We account for this effect by estimating the Poissonian probability, *P*, that a given optical counterpart is spurious alignment following the method of Downes et al.

[1] http://saci.ucolick.org/verdi/public/index.html

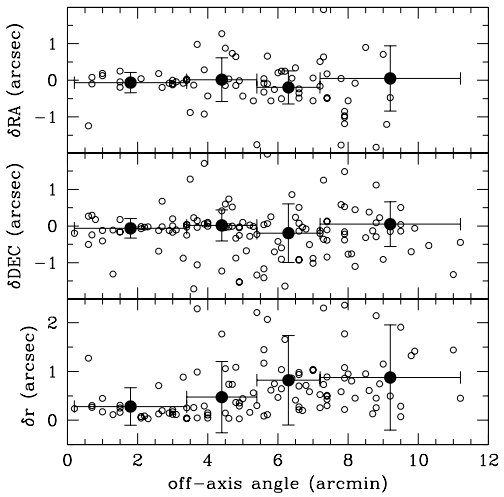

Figure 1. X-ray/optical positional offset in RA (upper panel), Dec. (middle panel) and total angular distance (lower panel) against X-ray off-axis angle. The filled points represent the mean offset within different off-axis angle bins. The horizontal error bar corresponds to the width of each bin, while the vertical error bar is the 1σ rms. The width of the bins varies so that each of them includes about 25 X-ray/optical pairs.

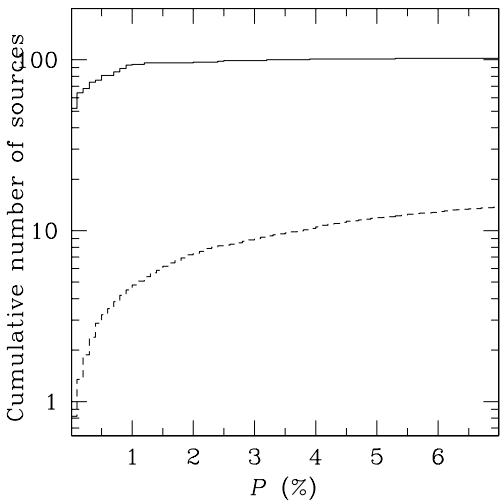

Figure 2. Number of optical identifications as a function of probability cut-off P for the full-band sample. The continuous histogram is for the real X-ray catalogue. The dashed line corresponds to the mean of 500 mock X-ray catalogues as described in the text.

(1986). Given the surface density of objects brighter than m, $\Sigma(<m)$, the expected number of candidates within r is $\mu = \pi r^2\,\Sigma(<m)$. Assuming that source positions are Poissonian, the probability of at least one object brighter than m within radius r is $P = 1 - \exp(-\mu)$. In practice one has to apply a cut-off in P to limit the optical identifications to those candidates that are least likely to be spurious alignments.

The probability P, however, is estimated under the assumption that the source positions are uniformly distributed within the surveyed area. For the real clustered distribution of optical sources, we assess the fraction of spurious optical identifications for different probability cut-offs using mock X-ray catalogues constructed by randomizing the positions of the X-ray sources within the area covered by the *Chandra* observations. The optical identification method is performed on the mock catalogues using the same criteria (e.g. matching radius) as for the real sources. This procedure is repeated 500 times. When constructing random X-ray catalogues we maintain the spatial distribution of the sources due to both vignetting and real clustering. This is accomplished by applying offsets in the range 30–60 arcsec to the X-ray source positions around their original centroid.

Fig. 2 plots the cumulative distribution of optical identifications for the full-band X-ray selected sample (using the matching radius scheme described above) as a function of probability cut-off. Also shown in Fig. 2 is the expected number of spurious counterparts estimated as described above. This figure shows that the number of optically identified sources reaches a plateau at $P \approx 1.5$ per cent while the spurious identification rate further increases with P. Based on Fig. 2, we adopt a cut-off probability $P < 2$ per cent for optical identification in the case of off-axis angles <6 arcmin. Because of the degradation of the positional accuracy at larger off-axis angles, we relax the probability cut-off to $P < 4$ for sources with $\theta > 6$ arcmin. This is to minimize the fraction of missed optical identifications because of the poor X-ray positions. For an optical source with $R_{\rm AB} = 24.5$ mag the probabilities $P < 2$ and $P < 4$ per cent correspond to maximum separations between the optical and X-ray centroids of about 1 and 1.5 arcsec, respectively. Repeating the simulations above using the off-axis-dependent identification scheme, we estimate a spurious fraction of about 4.5 per cent. The choice of P is a trade-off between maximum number of optical counterparts and minimum contamination rate. Similar results and false identification rates are obtained for the soft, hard and ultrahard samples.

For X-ray sources with no optical identification to the DEEP2 magnitude limit or outside the DEEP2 field of view, we use the CFHTLS to search for fainter optical counterparts applying the same selection criteria described above. Moreover, a number of optically faint X-ray sources lie in the gaps between the CCDs of the MegaCam mosaic. For these sources we use the Steidel et al. (2003) deep optical imaging to search for optical identifications. Considering sources fainter than the DEEP2 magnitude limit increases the spurious fraction rate by about 2 per cent. A total of 29 sources are identified with galaxies from the CFHTLS or the Steidel et al. (2003) survey. Table 1 summarizes the identification statistics for different X-ray selected subsamples. Table 2 presents the optical properties of the GWS X-ray sources as well as the source of optical photometry.

4 REDSHIFT ESTIMATION

Spectroscopic redshifts are available for a total of 51 sources. These are classified into three groups on the basis of their optical spectroscopic properties (primarily from DEEP1 and DEEP2)

Table 1. Optical and spectroscopic identification statistics. The columns are (1): X-ray subsample; (2) total number of X-ray sources; (3) number of optical counterparts; (4) number of spectroscopic identifications; (5) number of sources with photometric redshift determination only (i.e. not spectroscopic z); (6) number of sources with optical counterparts for which photometric redshift estimations were not possible; (7) number of blank fields.

X-ray subsample	Total number	Optical IDs	Spectro z only	Photo z only	Optical ID, no. z	No. ID
Total	155	128	51	36	42	27
Soft	121	102	42	27	33	19
Hard	97	83	37	24	22	14
Ultrahard	44	40	23	10	7	4

Table 2. *Chandra* GWS X-ray/optical catalogue. Column (1): source catalogue number; column (2): X-ray RA in J2000; column (3): X-ray Dec. in J2000; column (4): X-ray/optical centroid offset in arcsec; column (5): per cent probability the optical counterpart is spurious alignment; column (6): R_{AB} magnitude and source of optical identification 1 = DEEP2, 2 = Steidel et al. (2003), 3 = CFHTLS; column (7): spectroscopic redshift and source catalogue 1 = DEEP2, 2 = DEEP (Weiner et al. 2005), 3: CFRS (Lilly et al. 1995), 4: Steidel et al. (2003), 5: SDSS; column (8): optical spectroscopic classification, NL = narrow emission lines, BL = broad emission lines, AB = absorption lines, UNCL = no classification available, STAR = Galactic star; column (9): photometric redshift; column (10): N_H in units of 10^{22} cm^{-2}; column (11): unobscured 0.5–10 keV X-ray luminosity in erg s^{-1}; column (12): flags, fshu = source detected at $<4 \times 10^{-6}$ probability in this band, where the bands are f = full, s = soft, h = hard, u = ultrahard.

Cat. no. (1)	α_X (J2000) (2)	δ_X (J2000) (3)	δ_{OX} (arcsec) (4)	P (per cent) (5)	R_{AB} (mag) (6)	z_{spec} (7)	Class (8)	z_{phot} (9)	N_H (10^{22} cm^{-2}) (10)	L_X(0.5–10 keV) (10^{43} erg s^{-1}) (11)	Flags (12)
c1	$14^h16^m42^s.10$	$+52°31'42''.81$	1.36	0.29	20.95[1]	0.605[1]	NL	$0.490^{+0.04}_{-0.04}$	$0.41^{+0.45}_{-0.28}$	6.45	fshu
c2	$14^h16^m43^s.50$	$+52°29'02''.83$	0.00	0.24	24.42[3]	–	–	–	<2.40	3.47	f
c3	$14^h16^m44^s.03$	$+52°30'10''.40$	0.41	0.12	22.62[1]	–	–	–	$2.87^{+3.16}_{-2.23}$	8.82	fsh
c4	$14^h16^m45^s.39$	$+52°29'05''.60$	0.36	0.03	21.20[1]	1.630[1]	BL	$0.070^{+0.1}_{-0.04}$	<1.49	19.85	fsh
c5	$14^h16^m46^s.99$	$+52°30'00''.79$	–	–	<26.00	–	–	–	$4.49^{+3.85}_{-3.17}$	6.23	fs
c6	$14^h16^m48^s.80$	$+52°25'58''.04$	0.73	0.08	20.84[1]	–	–	–	<0.84	6.77	fs
c7	$14^h16^m49^s.46$	$+52°25'30''.75$	0.06	<0.01	20.00[1]	–	–	–	$0.17^{+0.43}_{-0.17}$	91.80	fshu
c8	$14^h16^m51^s.21$	$+52°20'47''.00$	1.35	0.29	20.70[1]	0.808[2]	BL	$0.980^{+0.17}_{-0.36}$	<0.32	9.48	fsh
c9	$14^h16^m52^s.03$	$+52°27'00''.54$	0.79	0.64	23.47[1]	–	–	$0.770^{+0.06}_{-0.07}$	$2.72^{+4.03}_{-2.06}$	9.06	fsh
c10	$14^h16^m53^s.46$	$+52°21'05''.54$	–	–	<24.50	–	–	–	$2.50^{+1.44}_{-1.21}$	23.17	fsh
c11	$14^h16^m53^s.82$	$+52°21'23''.79$	0.00	0.01	22.06[3]	–	–	$0.620^{+0.05}_{-0.06}$	$10.05^{+7.44}_{-4.17}$	2.62	fhu
c12	$14^h16^m58^s.53$	$+52°24'12''.60$	–	–	<26.00	–	–	–	$9.57^{+6.96}_{-4.99}$	7.59	fsh
c13	$14^h16^m59^s.11$	$+52°22'41''.88$	–	–	<26.00	–	–	–	$28.77^{+36.66}_{-20.29}$	5.34	f
c14	$14^h16^m59^s.26$	$+52°34'36''.04$	0.00	1.23	25.03[3]	–	–	–	$40.30^{+75.73}_{-23.82}$	9.18	fh
c15	$14^h17^m00^s.03$	$+52°23'04''.41$	0.97	2.09	24.38[1]	–	–	$1.270^{+0.16}_{-0.08}$	$16.84^{+89.76}_{-11.48}$	3.58	fh
c16	$14^h17^m00^s.69$	$+52°19'18''.58$	0.34	0.01	20.25[1]	–	–	–	<1.15	38.42	fsh
c17	$14^h17^m04^s.19$	$+52°21'40''.46$	1.09	0.82	22.59[1]	–	–	$0.750^{+0.04}_{-0.04}$	$7.49^{+2.78}_{-2.25}$	3.96	fshu
c18	$14^h17^m04^s.26$	$+52°24'53''.78$	0.44	0.01	19.42[1]	0.281[1]	NL	$0.370^{+0.08}_{-0.08}$	$8.82^{+3.15}_{-2.11}$	1.04	fshu
c19	$14^h17^m05^s.71$	$+52°31'46''.27$	0.76	0.87	23.73[1]	–	–	$2.200^{+0.32}_{-0.32}$	$20.58^{+42.17}_{-19.10}$	6.92	fh
c20	$14^h17^m05^s.75$	$+52°32'30''.62$	0.00	0.07	22.24[3]	–	–	–	<2.02	2.65	fs
c21	$14^h17^m08^s.49$	$+52°32'25''.40$	0.00	2.03	25.59[3]	–	–	$0.920^{+0.19}_{-0.18}$	<1.01	0.32	fs
c22	$14^h17^m08^s.64$	$+52°29'29''.72$	–	–	<26.00	–	–	$1.120^{+0.13}_{-0.4}$	<1.19	1.63	fs
c23	$14^h17^m08^s.97$	$+52°27'09''.00$	0.51	0.04	20.61[1]	0.532[1]	AB	$0.540^{+0.03}_{-0.04}$	$3.36^{+2.59}_{-1.89}$	0.34	f
c24	$14^h17^m10^s.28$	$+52°34'33''.95$	2.96	<0.01	21.55[2]	–	–	–	$3.99^{+1.98}_{-1.56}$	1.14	fshu
c25	$14^h17^m10^s.62$	$+52°28'28''.73$	0.24	0.02	22.02[1]	–	–	–	<0.08	0.13	fsh
c26	$14^h17^m11^s.05$	$+52°28'37''.66$	–	–	<26.00	–	–	–	$1.19^{+1.86}_{-1.19}$	2.89	fshu
c27	$14^h17^m11^s.12$	$+52°25'41''.95$	1.31	0.14	19.91[1]	0.418[4]	NL	–	<0.08	0.06	fs
c28	$14^h17^m11^s.64$	$+52°31'32''.12$	0.19	0.02	22.77[1]	0.835[1]	NL	$0.940^{+0.33}_{-0.05}$	<0.95	0.39	fs
c29	$14^h17^m11^s.88$	$+52°20'11''.61$	0.19	<0.01	19.79[1]	0.433[1]	NL	$0.600^{+0.05}_{-0.06}$	<0.04	4.76	fshu
c30	$14^h17^m12^s.90$	$+52°22'07''.53$	–	–	<26.00	–	–	–	$3.38^{+20.00}_{-3.38}$	1.20	f
c31	$14^h17^m14^s.35$	$+52°25'32''.98$	–	–	<26.00	–	–	–	$1.65^{+4.86}_{-1.65}$	1.39	fs
c32	$14^h17^m14^s.94$	$+52°34'20''.09$	0.00	3.32	24.49[3]	–	–	–	$26.68^{+97.17}_{-18.28}$	4.46	fh
c33	$14^h17^m15^s.07$	$+52°23'12''.33$	0.17	<0.01	21.32[1]	1.263[2]	BL	$1.700^{+0.34}_{-0.34}$	$0.02^{+0.63}_{-0.02}$	8.94	fshu
c34	$14^h17^m15^s.21$	$+52°26'49''.99$	1.17	0.32	21.43[1]	0.723[1]	NL	$0.740^{+0.07}_{-0.05}$	$5.51^{+2.15}_{-1.84}$	2.23	fshu
c35	$14^h17^m18^s.89$	$+52°27'43''.74$	1.06	1.17	23.47[1]	1.211[1]	NL	$1.120^{+0.11}_{-0.08}$	<2.15	0.87	f
c36	$14^h17^m19^s.00$	$+52°30'51''.04$	–	–	<26.00	–	–	–	<3.56	0.83	fs
c37	$14^h17^m19^s.32$	$+52°27'55''.54$	0.36	0.19	23.72[1]	1.208[1]	NL	$1.130^{+0.19}_{-0.06}$	$0.53^{+3.26}_{-0.53}$	0.97	fs
c38	$14^h17^m20^s.07$	$+52°25'00''.37$	0.10	0.02	24.03[1]	–	–	$0.460^{+0.09}_{-0.04}$	$0.33^{+0.54}_{-0.33}$	0.20	fsh
c39	$14^h17^m20^s.43$	$+52°29'11''.68$	0.00	0.49	25.83[3]	–	–	–	<2.27	1.31	fs
c40	$14^h17^m22^s.98$	$+52°31'43''.50$	0.12	<0.01	21.30[1]	0.465[1]	NL	$0.580^{+0.05}_{-0.04}$	<0.58	0.24	fsh
c41	$14^h17^m23^s.43$	$+52°31'53''.54$	0.10	<0.01	21.26[1]	0.484[1]	BL	$0.660^{+0.06}_{-0.07}$	<0.24	1.13	fshu
c42	$14^h17^m23^s.63$	$+52°25'55''.05$	0.38	0.22	23.54[1]	–	–	–	$24.61^{+26.83}_{-15.05}$	2.08	fh
c43	$14^h17^m24^s.30$	$+52°32'29''.61$	0.43	0.19	23.26[1]	0.902[1]	NL	$0.830^{+0.09}_{-0.04}$	<5.84	0.39	fs
c44	$14^h17^m24^s.62$	$+52°30'24''.55$	0.10	<0.01	19.99[1]	0.482[1]	BL	$0.990^{+0.17}_{-0.46}$	<0.12	3.01	fshu
c45	$14^h17^m25^s.28$	$+52°35'12''.08$	–	–	<26.00	–	–	$0.590^{+0.57}_{-0.24}$	<0.90	0.09	f
c46	$14^h17^m25^s.37$	$+52°35'44''.19$	–	–	<26.00	–	–	–	$4.76^{+4.15}_{-2.99}$	6.53	fsh
c47	$14^h17^m27^s.08$	$+52°29'11''.97$	0.09	0.01	23.63[1]	–	–	$4.528^{+0.45}_{-0.45}$	<0.44	5.61	fshu
c48	$14^h17^m27^s.31$	$+52°31'31''.33$	0.00	0.68	25.68[3]	–	–	–	$6.71^{+15.11}_{-6.09}$	1.81	fs
c49	$14^h17^m29^s.02$	$+52°35'53''.59$	0.00	2.99	24.96[3]	–	–	–	$0.05^{+0.77}_{-0.05}$	0.26	fs
c50	$14^h17^m29^s.97$	$+52°27'47''.62$	0.08	0.03	25.32[1]	–	–	$0.610^{+0.21}_{-0.07}$	$0.29^{+0.40}_{-0.29}$	1.48	fshu

Table 2 – *continued*

Cat. No. (1)	α_X (J2000) (2)	δ_X (J2000) (3)	δ_{OX} (arcsec) (4)	P (per cent) (5)	R_{AB} (mag) (6)	z_{spec} (7)	Class (8)	z_{phot} (9)	N_H (10^{22} cm^{-2}) (10)	L_X (0.5–10 keV) (10^{43} erg s^{-1}) (11)	Flags (12)
c51	$14^h17^m30^s.62$	$+52°22'42''.95$	0.39	0.51	24.79[1]	–	–	$1.160^{+0.12}_{-0.08}$	$1.49^{+2.93}_{-1.49}$	1.51	fs
c52	$14^h17^m30^s.66$	$+52°23'02''.21$	–	–	<26.00	–	–	–	<0.89	1.72	fs
c53	$14^h17^m30^s.72$	$+52°23'05''.35$	0.45	<0.01	25.72[2]	–	–	–	<0.56	0.50	fs
c54	$14^h17^m30^s.87$	$+52°28'18''.22$	0.00	0.79	25.74[3]	–	–	$0.550^{+0.39}_{-0.22}$	$6.10^{+5.35}_{-3.15}$	0.42	fh
c55	$14^h17^m32^s.65$	$+52°32'02''.97$	0.12	0.01	22.83[1]	0.986[1]	NL	$0.820^{+0.1}_{-0.03}$	$0.72^{+0.73}_{-0.66}$	5.53	fshu
c56	$14^h17^m33^s.64$	$+52°20'38''.86$	2.44	0.96	20.94[1]	–	–	$0.530^{+0.05}_{-0.06}$	$14.30^{+14.65}_{-6.28}$	1.55	fh
c57	$14^h17^m33^s.83$	$+52°33'49''.03$	0.16	<0.01	21.18[1]	0.550[1]	NL	$0.640^{+0.04}_{-0.07}$	$2.16^{+1.19}_{-0.92}$	0.84	fshu
c58	$14^h17^m34^s.02$	$+52°24'56''.12$	–	–	<26.00	–	–	–	$101.21^{+255.55}_{-78.05}$	4.46	fh
c59	$14^h17^m34^s.41$	$+52°31'06''.63$	0.14	<0.01	19.49[1]	0.271[1]	AB	$0.290^{+0.07}_{-0.03}$	$0.02^{+0.42}_{-0.02}$	0.05	fsh
c60	$14^h17^m34^s.87$	$+52°28'10''.45$	0.08	<0.01	20.82[1]	1.223[2]	BL	$0.460^{+0.14}_{-0.07}$	<1.06	14.08	fshu
c61	$14^h17^m35^s.98$	$+52°30'29''.55$	0.10	<0.01	19.87[1]	0.985[3]	BL	$0.130^{+0.12}_{-0.09}$	<0.04	69.66	fshu
c62	$14^h17^m36^s.32$	$+52°30'16''.70$	0.14	0.07	24.62[1]	0.969[4]	NL	–	$3.26^{+6.46}_{-3.26}$	0.53	f
c63	$14^h17^m36^s.39$	$+52°35'44''.08$	0.49	0.36	23.81[1]	–	–	$0.380^{+0.07}_{-0.19}$	<0.38	0.18	fs
c64	$14^h17^m36^s.89$	$+52°24'29''.80$	0.23	0.02	22.14[1]	2.125[4]	BL	$2.056^{+0.31}_{-0.76}$	<1.04	13.84	fshu
c65	$14^h17^m37^s.38$	$+52°29'21''.37$	–	–	<26.00	–	–	–	$68.09^{+59.75}_{-36.37}$	10.63	fhu
c66	$14^h17^m38^s.76$	$+52°34'13''.47$	0.63	0.89	24.18[1]	–	–	–	<1.54	1.35	fs
c67	$14^h17^m38^s.88$	$+52°23'32''.92$	0.23	0.01	21.22[1]	2.148[1]	BL	$1.691^{+0.12}_{-0.2}$	<0.69	51.50	fshu
c68	$14^h17^m39^s.06$	$+52°28'43''.78$	0.43	0.65	24.92[1]	–	–	–	<0.01	0.79	fs
c69	$14^h17^m39^s.31$	$+52°28'50''.16$	0.12	0.01	23.26[1]	0.997[2]	UNCL	–	<0.01	0.99	fh
c70	$14^h17^m39^s.56$	$+52°36'19''.72$	0.98	0.67	22.97[1]	–	–	–	$2.27^{+2.66}_{-1.95}$	5.93	fs
c71	$14^h17^m41^s.44$	$+52°35'45''.38$	0.73	0.54	23.27[1]	–	–	$1.480^{+0.38}_{-0.38}$	$19.64^{+11.17}_{-8.75}$	7.26	fsh
c72	$14^h17^m41^s.90$	$+52°28'23''.26$	0.10	<0.01	21.55[1]	1.148[1]	BL	$0.860^{+0.13}_{-0.03}$	$1.16^{+0.56}_{-0.49}$	38.47	fshu
c73	$14^h17^m42^s.86$	$+52°22'35''.21$	–	–	<26.00	–	–	–	<0.01	1.11	s
c74	$14^h17^m43^s.28$	$+52°20'23''.10$	0.81	0.01	17.20[1]	0.097[5]	AB	$0.160^{+0.1}_{-0.03}$	$0.15^{+0.97}_{-0.15}$	0.005	fs
c75	$14^h17^m45^s.47$	$+52°29'51''.17$	0.03	<0.01	22.47[1]	0.873[1]	NL	$0.830^{+0.07}_{-0.05}$	$20.77^{+9.40}_{-6.66}$	5.66	fshu
c76	$14^h17^m45^s.70$	$+52°28'01''.91$	1.25	0.51	21.99[1]	0.432[2]	NL	$0.400^{+0.06}_{-0.08}$	$0.15^{+0.40}_{-0.15}$	0.41	fshu
c77	$14^h17^m45^s.99$	$+52°30'32''.32$	0.09	<0.01	22.93[1]	0.985[1]	NL	$0.770^{+0.05}_{-0.03}$	$3.89^{+3.68}_{-3.46}$	12.28	fshu
c78	$14^h17^m46^s.17$	$+52°25'26''.65$	0.32	0.10	23.47[1]	–	–	–	$13.79^{+84.41}_{-11.41}$	2.08	f
c79	$14^h17^m46^s.73$	$+52°28'58''.18$	0.00	0.62	27.74[3]	–	–	–	$3.36^{+6.94}_{-3.36}$	1.23	fs
c80	$14^h17^m47^s.01$	$+52°25'12''.07$	0.75	0.39	22.54[1]	0.749[1]	NL	$0.700^{+0.05}_{-0.03}$	$0.05^{+358.60}_{-0.05}$	0.11	fh
c81	$14^h17^m47^s.06$	$+52°28'16''.46$	–	–	<26.00	–	–	–	$1.03^{+8.21}_{-1.03}$	2.17	fsh
c82	$14^h17^m47^s.43$	$+52°35'10''.39$	0.65	0.44	23.21[1]	2.746[4]	BL	$2.930^{+0.26}_{-0.26}$	$0.15^{+3.42}_{-0.15}$	25.79	fsh
c83	$14^h17^m49^s.21$	$+52°28'03''.28$	0.37	0.14	23.08[1]	0.996[1]	NL	$0.880^{+0.28}_{-0.02}$	$3.63^{+14.10}_{-3.63}$	0.66	fh
c84	$14^h17^m49^s.23$	$+52°28'11''.38$	0.17	0.04	23.83[1]	0.998[2]	NL	$0.830^{+0.07}_{-0.06}$	$0.41^{+0.88}_{-0.41}$	6.62	fsh
c85	$14^h17^m49^s.72$	$+52°31'43''.46$	–	–	<26.00	–	–	–	$3.04^{+4.88}_{-3.04}$	5.57	fshu
c86	$14^h17^m50^s.19$	$+52°36'01''.15$	0.00	1.68	26.22[3]	–	–	$1.100^{+0.25}_{-0.18}$	<1.44	1.51	fs
c87	$14^h17^m50^s.56$	$+52°23'39''.98$	–	–	<26.00	–	–	–	$14.51^{+27.12}_{-12.84}$	7.42	fsh
c88	$14^h17^m50^s.87$	$+52°36'32''.47$	0.57	0.73	24.18[1]	–	–	–	$0.01^{+0.44}_{-0.01}$	0.01	fs
c89	$14^h17^m51^s.00$	$+52°25'34''.13$	0.02	<0.01	20.86[1]	0.431[1]	AB	–	$21.92^{+20.57}_{-10.75}$	0.78	fhu
c90	$14^h17^m51^s.18$	$+52°23'10''.96$	0.17	<0.01	19.83[1]	–	–	$0.460^{+0.03}_{-0.08}$	$0.35^{+0.35}_{-0.24}$	0.74	fshu
c91	$14^h17^m51^s.78$	$+52°30'46''.36$	0.00	0.64	24.36[3]	–	–	$1.250^{+0.12}_{-0.23}$	$2.25^{+4.76}_{-2.25}$	1.12	fs
c92	$14^h17^m52^s.45$	$+52°28'53''.14$	0.14	0.02	23.92[1]	–	–	$1.080^{+0.08}_{-0.08}$	$20.46^{+20.36}_{-16.40}$	4.46	fhu
c93	$14^h17^m52^s.96$	$+52°28'38''.53$	0.43	0.04	21.39[1]	0.671[1]	NL	$0.710^{+0.07}_{-0.05}$	<2.12	0.07	f
c94	$14^h17^m53^s.13$	$+52°20'50''.02$	0.00	1.72	22.67[3]	–	–	$0.830^{+0.07}_{-0.05}$	$0.19^{+2.68}_{-0.19}$	0.40	f
c95	$14^h17^m53^s.72$	$+52°34'46''.34$	0.18	0.01	22.38[1]	0.719[1]	NL	$0.800^{+0.08}_{-0.06}$	$25.63^{+22.09}_{-9.68}$	4.85	fhu
c96	$14^h17^m53^s.99$	$+52°30'33''.94$	0.17	0.06	24.33[1]	0.998[2]	UNCL	$0.830^{+0.12}_{-0.06}$	$4.76^{+4.35}_{-3.15}$	1.09	fsh
c97	$14^h17^m54^s.25$	$+52°31'23''.37$	0.16	0.06	24.20[1]	–	–	$0.810^{+0.06}_{-0.1}$	<0.26	0.86	fsh
c98	$14^h17^m54^s.58$	$+52°34'37''.95$	0.53	0.29	23.44[1]	0.948[1]	NL	$0.850^{+0.3}_{-0.04}$	$28.07^{+35.33}_{-14.80}$	2.82	fh
c99	$14^h17^m55^s.27$	$+52°35'32''.96$	0.35	0.08	22.55[1]	3.199[4]	UNCL	$2.930^{+0.26}_{-0.26}$	$1.35^{+8.08}_{-1.35}$	16.94	fsh
c100	$14^h17^m56^s.76$	$+52°24'00''.07$	0.24	<0.01	25.86[2]	–	–	–	$2.21^{+3.26}_{-2.21}$	3.72	fsh
c101	$14^h17^m56^s.87$	$+52°31'24''.49$	0.09	0.01	23.98[1]	–	–	$0.740^{+0.09}_{-0.07}$	$0.01^{+0.43}_{-0.01}$	1.01	fshu
c102	$14^h17^m56^s.92$	$+52°31'18''.47$	0.00	0.44	25.10[3]	–	–	–	$2.23^{+43.75}_{-2.23}$	0.53	f
c103	$14^h17^m57^s.12$	$+52°26'30''.98$	0.68	<0.01	24.45[2]	–	–	–	$7.74^{+3.00}_{-2.57}$	14.69	fshu
c104	$14^h17^m57^s.48$	$+52°31'06''.92$	0.00	0.19	24.89[3]	3.026[4]	UNCL	$3.150^{+0.24}_{-0.24}$	$20.02^{+20.05}_{-15.41}$	14.62	fshu
c105	$14^h17^m57^s.51$	$+52°25'46''.45$	0.15	0.02	23.34[1]	0.995[1]	NL	–	$1.29^{+1.67}_{-1.29}$	1.51	fsh

Table 2 – *continued*

Cat No. (1)	α_X (J2000) (2)	δ_X (J2000) (3)	δ_{OX} (arcsec) (4)	P (per cent) (5)	R_{AB} (mag) (6)	z_{spec} (7)	Class (8)	z_{phot} (9)	N_H (10^{22} cm^{-2}) (10)	L_X(0.5–10 keV) (10^{43} erg s^{-1}) (11)	Flags (12)
c106	$14^h17^m58^s.17$	$+52°31'33''.63$	0.00	1.64	23.56[3]	–	–	–	$0.12^{+4.13}_{-0.12}$	0.42	f
c107	$14^h17^m58^s.20$	$+52°21'53''.24$	0.00	0.32	22.89[3]	–	–	$0.940^{+0.16}_{-0.08}$	$0.65^{+1.79}_{-0.65}$	1.80	fsh
c108	$14^h17^m58^s.97$	$+52°31'38''.89$	0.20	0.02	22.71[1]	0.644[4]	BL	$0.765^{+0.07}_{-0.08}$	$0.29^{+0.38}_{-0.29}$	2.17	fshu
c109	$14^h17^m59^s.32$	$+52°24'20''.30$	0.22	0.07	23.78[1]	–	–	$0.320^{+0.09}_{-0.12}$	<0.41	0.04	fs
c110	$14^h18^m00^s.08$	$+52°22'23''.26$	0.24	0.20	24.63[1]	–	–	$1.170^{+0.12}_{-0.13}$	$4.29^{+4.74}_{-4.29}$	11.05	fshu
c111	$14^h18^m00^s.41$	$+52°28'22''.22$	0.61	0.55	23.73[1]	–	–	–	$3.11^{+8.05}_{-3.11}$	2.33	fh
c112	$14^h18^m00^s.43$	$+52°36'10''.11$	0.00	1.16	26.23[3]	–	–	–	<1.56	5.55	fsh
c113	$14^h18^m01^s.15$	$+52°29'41''.78$	0.06	<0.01	23.04[1]	2.907[4]	BL	$2.930^{+0.26}_{-0.26}$	<6.27	5.42	fs
c114	$14^h18^m01^s.37$	$+52°31'50''.77$	–	–	<26.00	–	–	$1.090^{+0.1}_{-0.09}$	$10.21^{+14.04}_{-7.13}$	1.20	fh
c115	$14^h18^m01^s.67$	$+52°28'00''.66$	0.02	<0.01	24.67[1]	–	–	–	$0.88^{+5.02}_{-0.88}$	0.74	fs
c116	$14^h18^m02^s.00$	$+52°35'14''.53$	0.32	<0.01	19.93[1]	1.497[1]	BL	$2.879^{+0.29}_{-0.31}$	<2.57	111.24	fshu
c117	$14^h18^m02^s.41$	$+52°21'32''.36$	0.00	0.01	18.86[3]	–	–	$0.230^{+0.09}_{-0.05}$	<0.27	0.05	fsh
c118	$14^h18^m02^s.93$	$+52°35'47''.11$	0.00	0.26	24.97[3]	–	–	–	$0.59^{+1.42}_{-0.59}$	8.09	fshu
c119	$14^h18^m04^s.55$	$+52°36'33''.15$	0.43	0.28	23.57[1]	–	–	$0.810^{+0.29}_{-0.04}$	$1.01^{+0.61}_{-0.54}$	4.81	fshu
c120	$14^h18^m04^s.90$	$+52°27'40''.14$	0.18	0.07	24.30[1]	–	–	$0.780^{+0.05}_{-0.08}$	$0.15^{+0.68}_{-0.15}$	0.79	fsh
c121	$14^h18^m05^s.30$	$+52°25'10''.63$	0.80	1.42	24.44[1]	–	–	$0.770^{+0.31}_{-0.07}$	$0.77^{+1.23}_{-0.77}$	0.82	fsh
c122	$14^h18^m06^s.51$	$+52°33'58''.67$	0.84	0.72	23.19[1]	–	–	–	$1.29^{+4.35}_{-1.29}$	1.26	fs
c123	$14^h18^m07^s.07$	$+52°25'23''.41$	–	–	<26.00	–	–	$0.750^{+0.4}_{-0.07}$	$1.78^{+1.07}_{-1.00}$	2.49	fsh
c124	$14^h18^m07^s.33$	$+52°30'30''.52$	0.85	0.51	22.58[1]	0.990[3]	NL	$0.850^{+0.08}_{-0.07}$	<13.12	0.10	s
c125	$14^h18^m08^s.06$	$+52°27'50''.36$	–	–	<26.00	–	–	–	<12.52	1.09	f
c126	$14^h18^m08^s.94$	$+52°31'50''.84$	–	–	<26.00	–	–	–	$339.29^{+271.69}_{-196.63}$	34.55	f
c127	$14^h18^m09^s.12$	$+52°28'04''.04$	–	–	<26.00	–	–	–	$6.71^{+6.10}_{-3.67}$	6.98	fshu
c128	$14^h18^m11^s.26$	$+52°30'11''.48$	0.86	1.12	23.79[1]	2.910[4]	UNCL	$3.090^{+0.22}_{-0.22}$	$15.47^{+45.56}_{-15.47}$	6.54	fs
c129	$14^h18^m12^s.16$	$+52°28'00''.29$	–	–	<26.00	–	–	–	$4.00^{+4.26}_{-3.29}$	3.47	fs
c130	$14^h18^m13^s.19$	$+52°31'13''.47$	–	–	<26.00	–	–	$0.950^{+0.27}_{-0.07}$	$0.68^{+1.15}_{-0.68}$	1.76	fsh
c131	$14^h18^m13^s.33$	$+52°24'14''.90$	0.00	1.45	26.81[3]	–	–	$1.230^{+0.15}_{-0.08}$	$1.07^{+3.37}_{-1.07}$	1.53	fs
c132	$14^h18^m13^s.96$	$+52°26'24''.79$	–	–	<26.00	–	–	–	$23.97^{+24.61}_{-15.99}$	5.17	fh
c133	$14^h18^m14^s.27$	$+52°28'10''.99$	1.02	0.49	22.22[1]	2.818[4]	BL	$2.552^{+0.25}_{-0.26}$	<1.65	8.47	fs
c134	$14^h18^m15^s.36$	$+52°32'47''.61$	0.00	1.29	24.28[3]	–	–	–	$0.87^{+1.57}_{-0.87}$	0.93	fs
c135	$14^h18^m16^s.29$	$+52°29'40''.30$	0.18	<0.01	20.07[1]	1.603[3]	BL	$1.700^{+0.34}_{-0.34}$	<0.27	34.39	fshu
c136	$14^h18^m16^s.35$	$+52°25'24''.05$	0.61	0.83	24.18[1]	–	–	–	$0.58^{+1.45}_{-0.58}$	3.47	fsh
c137	$14^h18^m16^s.43$	$+52°33'29''.77$	0.12	0.03	24.22[1]	–	–	–	<1.53	0.29	fs
c138	$14^h18^m16^s.73$	$+52°23'07''.98$	0.75	0.57	23.37[1]	–	–	–	<0.32	1.23	fsh
c139	$14^h18^m18^s.04$	$+52°32'01''.28$	0.99	3.31	24.64[1]	–	–	$0.390^{+0.07}_{-0.12}$	$1.44^{+1.25}_{-0.99}$	0.17	fs
c140	$14^h18^m19^s.92$	$+52°21'15''.80$	–	–	<26.00	–	–	$1.062^{+0.11}_{-0.12}$	$9.76^{+16.59}_{-7.03}$	2.85	f
c141	$14^h18^m20^s.30$	$+52°33'51''.08$	1.85	3.51	23.15[1]	–	–	$2.200^{+0.32}_{-0.32}$	$0.02^{+4.52}_{-0.02}$	5.97	fs
c142	$14^h18^m21^s.37$	$+52°26'55''.46$	–	–	<26.00	–	–	–	<5.18	1.83	fs
c143	$14^h18^m21^s.39$	$+52°32'54''.31$	0.44	0.29	23.57[1]	–	–	–	$3.58^{+4.28}_{-3.22}$	0.82	fsh
c144	$14^h18^m21^s.79$	$+52°29'55''.82$	0.90	0.06	19.71[1]	0.000[3]	STAR	–	–	–	fs
c145	$14^h18^m22^s.08$	$+52°26'50''.20$	0.55	0.14	22.06[1]	–	–	$0.740^{+0.06}_{-0.04}$	$0.60^{+1.31}_{-0.60}$	0.64	fs
c146	$14^h18^m22^s.41$	$+52°36'07''.45$	1.31	3.83	24.15[1]	–	–	–	$0.57^{+1.13}_{-0.57}$	15.50	fshu
c147	$14^h18^m22^s.84$	$+52°27'10''.11$	1.54	0.07	18.26[1]	0.281[5]	AB	$0.530^{+0.04}_{-0.05}$	<0.08	0.04	fs
c148	$14^h18^m23^s.07$	$+52°21'14''.50$	0.00	0.73	23.84[3]	–	–	$1.050^{+0.06}_{-0.07}$	$10.50^{+7.59}_{-6.21}$	4.81	fh
c149	$14^h18^m24^s.97$	$+52°23'30''.55$	0.66	0.31	22.97[1]	–	–	$1.040^{+0.16}_{-0.08}$	$3.48^{+2.17}_{-2.10}$	17.92	fshu
c150	$14^h18^m25^s.52$	$+52°23'49''.48$	0.10	<0.01	22.51[1]	–	–	–	$0.31^{+0.91}_{-0.31}$	2.52	fshu
c151	$14^h18^m26^s.36$	$+52°28'18''.80$	0.81	0.68	23.00[1]	–	–	–	<0.79	7.16	fsh
c152	$14^h18^m26^s.44$	$+52°32'35''.01$	0.71	0.04	19.91[1]	–	–	$0.730^{+0.01}_{-0.01}$	<0.27	0.33	fs
c153	$14^h18^m26^s.51$	$+52°25'59''.70$	0.98	<0.01	24.65[2]	–	–	–	$12.00^{+10.85}_{-6.92}$	5.89	fsh
c154	$14^h18^m29^s.76$	$+52°27'09''.39$	0.56	0.15	22.48[1]	–	–	$0.720^{+0.05}_{-0.03}$	$6.36^{+4.97}_{-3.18}$	1.30	fh
c155	$14^h18^m30^s.24$	$+52°22'12''.14$	0.16	<0.01	20.83[1]	–	–	–	<0.13	107.14	fshu
c156	$14^h18^m32^s.87$	$+52°23'49''.48$	0.74	0.06	20.15[1]	–	–	–	<2.33	29.17	fsh
c157	$14^h18^m37^s.96$	$+52°20'34''.62$	–	–	<26.00	–	–	–	<1.52	2.53	s
c158	$14^h18^m38^s.18$	$+52°23'58''.55$	1.99	0.18	18.84[1]	1.118[5]	BL	$1.500^{+0.15}_{-0.17}$	<0.21	17.79	fsh

following methods described in Sarajedini et al. (2006): broad emission-line galaxies, narrow emission-line sources and systems with absorption lines. For broad emission-line AGN we adopt the criterion full width at half-maximum (FWHM) $> 1200\,\mathrm{km\,s^{-1}}$. We note that the low signal-to-noise ratio of some of the spectra and the small spectral window of the DEEP2 observations (6000–9500 Å) introduce some uncertainty in the classification scheme above. In addition to the above three groups, a number of sources in the sample cannot be classified because the optical spectra were not available for visual inspection.

For X-ray sources without spectroscopic identification, we estimate photometric redshifts exploiting the multiwaveband photometry (*ugriz*) of the CFHTLS. Determining photometric redshifts for X-ray sources is challenging because of the significant, if not dominant, AGN component contributing to the optical broad-band colours (e.g. Babbedge et al. 2004; Kitsionas et al. 2005). Recent studies, however, suggest that many moderate luminosity AGN ($\lesssim 10^{44}\,\mathrm{erg\,s^{-1}}$) as well as obscured X-ray sources have optical continuum emission that is dominated by stellar light, thus allowing galaxy templates to be used for photometric redshifts (Barger et al. 2003; Gandhi et al. 2004; Georgakakis et al. 2004; Georgakakis, Georgantopoulos & Akylas 2006).

We explore this possibility using the photometric redshift code of Gwyn (2001) based on a standard χ^2 minimization method. The galaxy templates are based on those of Coleman, Wu & Weedman (1980), providing spectral energy distributions (SEDs) for four main spectral galaxy types (E/S0, Sbc, Scd, Im), extended in the ultraviolet (UV) and IR wavelength regions using the GISSEL98 code (e.g. Bruzual & Charlot 1993). These are supplemented with the starburst SB2 and SB3 spectra from Kinney et al. (1996). Having only a small number of SEDs can cause aliasing in photometric redshifts. Therefore, a new template set has been created by smoothly interpolating between each of the six original spectra. This results in a total 51 SEDs from ellipticals (spectral classification 0) to extreme starbursts (spectral classification 1).

Fig. 3 compares the photometric and spectroscopic redshift estimates for the sources with available spectroscopic observations. With the exception of broad-line QSOs, there is fair agreement

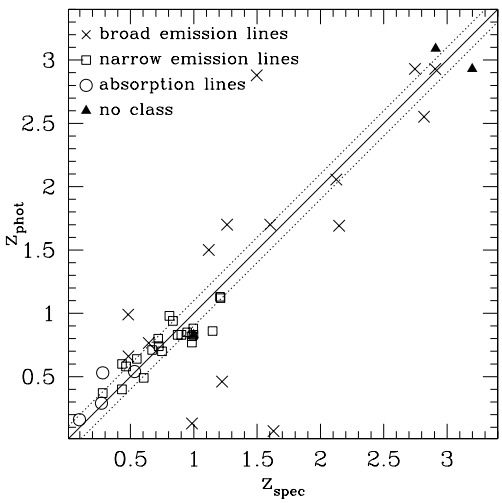

Figure 3. Photometric against spectroscopic redshift estimates for the X-ray sources with available spectroscopic observations. Circles are for sources with absorption-line spectra, squares correspond to systems with narrow emission-line spectra and crosses are broad-line AGNs. Triangles are sources with no classification.

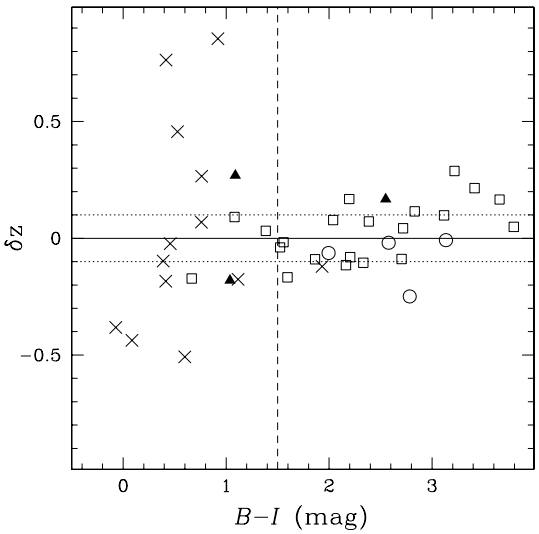

Figure 4. $\delta z = (z_{\rm phot} - z_{\rm spec})$ against DEEP2 $B - I$ colour. The symbols are the same as in Fig. 3.

between $z_{\rm spec}$ and $z_{\rm phot}$ with an rms scatter, after excluding broad-line AGN, $(1/N)\sum((z_{\rm phot} - z_{\rm spec})/(1 + z_{\rm spec}))^2 = 0.08$, where N is the total number of sources. This is further demonstrated in Fig. 4 plotting $\delta z = (z_{\rm phot} - z_{\rm spec})$ against $B - I$ colour. Sources bluer than $B - I \approx 1.5$ are dominated by broad-line QSOs with an rms scatter $\delta z/(1 - z_{\rm spec}) = 0.25$ (e.g. Barger et al. 2003; Kitsionas et al. 2005). For systems redder than this limit, however, the photometric redshifts are more reliable. To avoid erroneous redshift estimates in the analysis that follows, we use photometric redshifts only for sources with $B - I > 1.5$ mag.

In addition to the standard photometric redshift estimation above, we exploit the Lyman Break galaxy selection available for the GWS (Steidel et al. 2003, 2004) to determine the redshift of a small number of X-ray sources. This method has been shown to be very efficient in identifying galaxies in well-defined narrow redshift slices within the range $1.5 \lesssim z \lesssim 3$ with a low interloper rate. Here we use the BM, BX, C, D, M and MD Lyman Break galaxy selection criteria fully described in Steidel et al. (2003, 2004), which correspond, respectively, to redshifts 1.70 ± 0.34, 2.20 ± 0.34, 3.09 ± 0.22, 2.93 ± 0.26, 3.15 ± 0.24 and 2.79 ± 0.27. In our sample there are seven X-ray sources that fulfill one of the above selection criteria: 2 BX, 2 MD, 1 C, 1 D and 1 M.

The optical spectroscopic and photometric redshift information for the GWS sample is presented in Table 2. For the full and hard band samples Fig. 5 presents the optical magnitude distribution of sources with spectroscopic, photometric or no redshift information as well as sources without optical identification. The total number of sources in these groups for different X-ray selected samples is also shown in Table 1. The no-redshift class involves sources that are either too faint to estimate photometric redshifts, do not have CFHTLS data (e.g. CCD gaps) or have counterparts with $B - I <$ 1.5 mag and therefore unreliable redshift determination.

5 X-RAY SPECTRA

For the X-ray spectral analysis we use the XSPEC v11.3.1 package. The X-ray counts of each source are extracted using the 95 per cent encircled energy radius (1.5 keV) at the position of the source. The background is estimated using an annulus centered

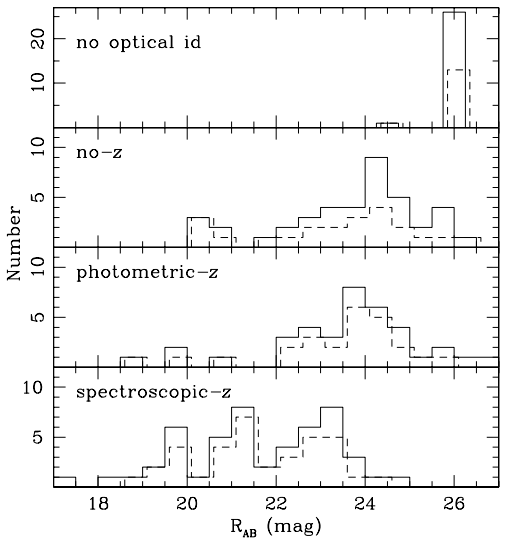

Figure 5. $R_{\rm AB}$ optical magnitude distribution for different subsamples of X-ray sources. The four panels from bottom to top plot, respectively, histograms for sources with spectroscopic redshifts, photometric redshifts only, without any redshift determination (but with an optical ID) and with no optical identification. Within each panel the continuous line corresponds to the full-band sample and the dashed line (offset to the right by 0.1 mag for clarity) represents the hard sample.

on the source with inner aperture size 1.5 times larger than the 95 per cent encircled energy radius and outer aperture 100 pixel greater. We fit the data adopting a power-law model absorbed by both an intrinsic column density at the redshift of the source and a Galactic column at $z = 0$ fixed to $N_{\rm H} = 1.3 \times 10^{20}\,{\rm cm}^{-2}$, appropriate for the EGS (WABS*ZWABS*POW). For the absorption we adopt the Wisconsin cross-sections (Morrison & McCammon 1983). For sources without spectroscopic or photometric redshift estimates (e.g. blank fields, sources with $B - I < 1.5$), we assume $z = 1.5$ to estimate the intrinsic $N_{\rm H}$. Adopting a different mean z in the range 1–2 for these systems, however, does not significantly modify our results and conclusions.

In the case of sources with small number of net counts ($\lesssim$200), we use the C-statistic technique (Cash 1979) specifically developed to extract information from low signal-to-noise ratio spectra. The data are grouped to have at least one count per bin. We attempt to constrain the intrinsic $N_{\rm H}$ by fixing the power-law index to $\Gamma = 1.8$. This value of Γ is selected to be in between the mean spectral index of radio loud ($\Gamma = 1.6$; Reeves & Turner 2000; Gambill et al. 2003) and radio quiet AGNs ($\Gamma \approx 1.9$; Nandra & Pounds 1994; Reeves & Turner 2000). Adopting a single fixed Γ for the spectral analysis is an approximation. We caution that our analysis will overestimate the $N_{\rm H}$ for sources with spectra intrinsically flatter than $\Gamma = 1.8$.

For sources with sufficient number of counts ($\gtrsim$ 200), we perform standard χ^2 spectral fitting. The data were grouped to have a minimum of 20 counts per bin to ensure that Gaussian statistics apply. For the χ^2 analysis we require that the source spectrum has at least 10 spectral bins. The WABS*ZWABS*POW model provides acceptable fits (i.e. reduced $\chi^2 \approx 1$) for all sources. The parameters estimated from the C-statistic and the χ^2 analysis are consistent within the errors.

For both the χ^2 and the C-statistic analysis the fit was performed in the 0.5–8 keV energy range where the sensitivity of the *Chandra* is the highest. The estimated errors correspond to the 90 per cent confidence level. The results of the X-ray spectral analysis are presented in Table 2.

6 THE MODEL

In this section, we describe the model we use to interpret the optical and X-ray properties of the GWS X-ray sources in the context of AGN evolution scenarios and different parametrizations for the intrinsic $N_{\rm H}$ distribution. Modelling of the data requires certain assumptions about the X-ray spectra of AGN, their luminosity function and its evolution with redshift as well as the relative fraction of obscured and unobscured systems.

We model the X-ray spectra of AGN adopting for simplicity an absorbed power-law SED with fixed exponent $\Gamma = 1.8$ and photoelectric absorption cross-sections as described by Morrison & McCammon (1983) for solar metallicity.

For the X-ray luminosity function (XLF) of AGNs and its evolution with redshift, we use the two different parametrizations presented by Miyaji, Hasinger & Schmidt (2000) and Ueda et al. (2003).

Miyaji et al. (2000) combined deep pencil-beam and shallow wide-area *ROSAT* surveys to estimate the XLF of unobscured AGNs in the rest-frame 0.5–2 keV energy band. We adopt the luminosity-dependent density evolution parametrization of the XLF proposed by Miyaji et al. (their model LDDE1). These authors argue that this model provides a better description of the observations compared to the pure density or luminosity evolution. In this picture AGNs evolve differentially with more luminous systems evolving faster than less luminous ones. Such a trend has also been proposed for the optical luminosity function of QSOs (e.g. Wisotzki 1998).

Ueda et al. (2003) estimated the AGN XLF in the rest-frame 2–10 keV energy range using a combination of hard-band (>2 keV) surveys conducted with *HEAO-1*, *ASCA* and *Chandra* missions. Here we adopt the luminosity-dependent density evolution of the luminosity function, which according to Ueda et al. provides a better fit to the data. In this parametrization the cut-off redshift, after which the evolution of AGN stops, increases with luminosity. We note that this is different from the Miyaji et al. (2000) luminosity-dependent density evolution, where it is the rate of evolution that changes with luminosity but not the cut-off redshift.

For the AGN $N_{\rm H}$ distribution, $f(N_{\rm H})$, we experiment with different parametrizations. The first model adopted here is the one estimated by Ueda et al. (2003) on the basis of observational data and for column densities in the range $10^{20} < N_{\rm H} < 10^{24}\,{\rm cm}^{-2}$. The interesting feature of their functional form is that the fraction of obscured AGNs drops with increasing luminosity. In that sense the Ueda et al. (2003) $f(N_{\rm H})$ does not strictly follow the unified model prescription (Antonucci 1993) where the only parameter determining the obscuring column density is the viewing angle to the observer. We also consider a set of models where $f(N_{\rm H})$ is a step function with a fixed ratio, $\mathcal{R}$, between absorbed ($N_{\rm H} > 10^{22}\,{\rm cm}^{-2}$) and unabsorbed ($N_{\rm H} < 10^{22}\,{\rm cm}^{-2}$) sources. We further assume that obscured and unobscured AGNs are distributed uniformly in the range $10^{20} < N_{\rm H} < 10^{22}\,{\rm cm}^{-2}$ and $10^{22} < N_{\rm H} < 10^{26}\,{\rm cm}^{-2}$, respectively. For the obscured systems, the above assumption is in fair agreement with the $N_{\rm H}$ distribution of Seyfert-2s estimated by Risaliti, Maiolino & Salvati (1999). These authors find that about 75 per cent of their sample has $N_{\rm H} > 10^{23}\,{\rm cm}^{-2}$ and at least 25 per cent has $N_{\rm H} > 10^{25}\,{\rm cm}^{-2}$. This set of models are consistent with the unified scheme with the ratio $\mathcal{R}$ related to the opening angle of the torus. Similar models but with a smooth transition between obscured and unobscured sources are presented by Treister et al. (2004). In this paper, we use models with $\mathcal{R} = 1$, 2, 3 and 4. We

note that $\mathcal{R} = 4$ is the locally estimated value for the fraction of obscured AGN (Maiolino & Rieke 1995).

7 RESULTS

In this section, we compare the observed redshift and column density distributions of the GWS sample against the predictions of the models above. To minimize incompleteness uncertainties due to either optically unidentified sources or systems without redshift determination (spectroscopic or photometric), we perform the comparison for the hard-band X-ray sources. The 2–10 keV sample has indeed sufficient number of sources to avoid poor statistics, while about 37 per cent of them (36 out of 97) are either blank fields or do not have a redshift estimate. Selection at the 2–10 keV band also provides samples that are less sensitive to obscuration and is therefore best suited for studies on the intrinsic fraction of obscured AGN. Finally, many groups have published results for the 2–10 keV spectral band and, therefore, choosing this energy range for the analysis facilitates comparison of our survey with previous samples. For the comparison with the models above, the AGN XLF is integrated in the redshift interval $z = 0$–5 for unobscured luminosities in the range $L_{\rm X}(2\text{–}10\,{\rm keV}) = 10^{42}$–$10^{46}\,{\rm erg\,s^{-1}}$. For each luminosity and redshift interval the distribution of AGNs to different columns is described by the $f(N_{\rm H})$ models discussed in the previous section. The predicted number density of objects in each $L_{\rm X}$, $N_{\rm H}$ and z bins are then folded through the sensitivity map of the EGS to estimate the number of AGNs to the flux limit of the survey.

7.1 The redshift distribution

Fig. 6 shows the redshift distribution of the hard-band sample. For sources without spectroscopic redshifts, we use the photometric redshift probability density distribution, instead of the primary solution only, to construct the histogram in Fig. 6. This approach guarantees that some of the uncertainties involved in the determination of photometric redshifts are factored into our analysis. For sources assigned photometric redshifts based on the Lyman Break galaxy selection (Steidel et al. 2003, 2004), we assume a Gaussian probability density distribution with a mean and a standard deviation appropriate for the selection criteria that each source fulfills (see Section 4).

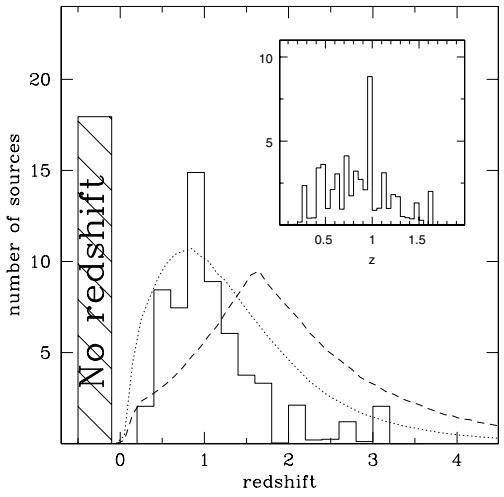

Figure 6. Redshift distribution of the hard X-ray selected sample. The hatched region shows the number of sources without spectroscopic identification. The dotted and dashed lines are the predictions of the Ueda et al. (2003) and Miyaji et al. (2000) XLFs, respectively. The inlet plot shows the same redshift distribution only for sources in the range $0 < z < 2$ using a narrower bin size to search for cosmic structures within the surveyed area.

A total of 36 hard X-ray selected sources (37 per cent of the sample) do not have spectroscopic or photometric redshift determination. These are shown with the hatched histogram in Fig. 6. Their optical magnitude distribution is presented in the two upper panels of Fig. 5. 14 of these 36 sources are blank fields and are most likely associated with $z > 1$ systems. The remaining 22 sources have a distribution that is skewed to fainter magnitudes in Fig. 5 compared to spectroscopically identified systems but similar to that of X-ray sources with photometric redshift determination. However, 17 of these 22 sources have $B - I < 1.5$ mag and are likely to be associated with high-z QSOs. Nevertheless, unless all spectroscopically unidentified sources are clustered in a narrow redshift slice, we do not expect them to drastically modify the position of the peak of the distribution in Fig. 6.

Also shown in Fig. 6 are the predictions of the two model XLFs presented in the previous section for the Ueda et al. (2003) $f(N_{\rm H})$. The adopted $N_{\rm H}$ distribution has only minor effects on the resulting redshift distribution and does not affect any of our conclusions. In Fig. 6, the Miyaji et al. (2000) prediction peaks at $z \approx 1.5$, higher than the observations. On the contrary, the Ueda et al. (2003) XLF produces a redshift distribution with a peak and overall shape in broad agreement with the data. There is, however, a larger fraction of $z \approx 1$ sources compared to the model prediction, suggesting a cosmic variance spike. This is more clearly demonstrated in the inlet plot of Fig. 6 which uses a narrower logarithmic redshift bin of 0.05. The full EGS sample will have a sufficiently wide field of view ($0.5\,{\rm deg^2}$) to address this issue. The Ueda et al. luminosity function also predicts a larger number of high-z systems compared to the observations. It is possible that some the X-ray sources without redshift determination will populate this high-z tail. We attempt to quantify the agreement between the observed and model distributions in Fig. 6, in the optimal case that the spectroscopically unidentified sources are distributed to redshift bins in such a way that the difference between the observed and model $N(z)$ is minimal. In the case of the Ueda et al. (2003) XLF we estimate a χ^2 test probability that the two distributions (model and observations) are drawn from the same parent population of about 99 per cent. For the Miyaji et al. (2000) model this exercise gives a probability of <1 per cent.

7.2 The column density distribution

Fig. 7 presents the $N_{\rm H}$ distribution of the hard X-ray selected sample. The fraction of obscured AGN ($N_{\rm H} > 10^{22}\,{\rm cm^{-2}}$) in this figure is estimated 48 ± 9 per cent. For sources without spectroscopic or photometric redshift estimates (e.g. blank fields, sources with $B - I < 1.5$), we assume $z = 1.5$ to estimate the intrinsic $N_{\rm H}$. Adopting a different mean z in the range 1–2 for these systems, however, does not significantly modify the derived $N_{\rm H}$ distribution. For the blue ($B - I < 1.5$) X-ray sources, in particular, adopting the photometric reshifts estimated in Section 4, which suffer larger uncertainties compared to redder sources, also does not change the results presented here. In the case of optically redder X-ray sources with $B - I > 1.5$, for which reliable photometric redshifts are available, the photo-z uncertainties have little impact on the observed distribution in Fig. 7. Assuming a redshift dependence of the rest-frame column density of the form $N_{\rm H} \propto (1 + z)^{2.65}$ (e.g. Barger et al. 2003) and a photo-z rms scatter $\delta z/(1 + z) = 0.08$ (see Section 4), we estimate $\delta \log N_{\rm H} = 0.09$, which is much smaller than the small photon statistics uncertainty.

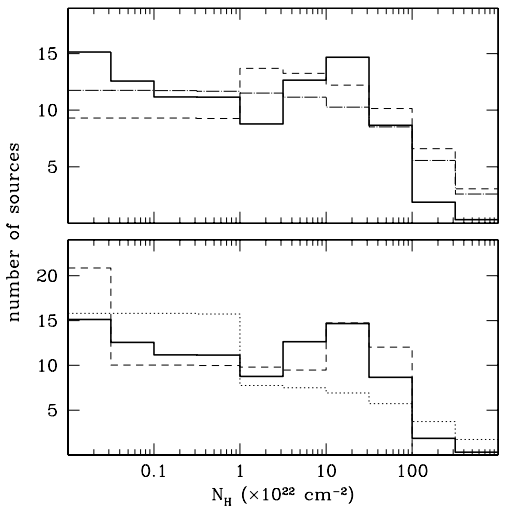

Figure 7. $N_{\rm H}$ distribution of the hard X-ray selected sample. In both panels the bold continuous line is the observed distribution. For clarity the comparison with the model predictions is split into two panels. Upper panel: comparison of the observations with the $\mathcal{R} = 2$, 3, and 4 models described in the text corresponding to the dash–dotted, dashed and dotted lines, respectively. Lower panel: comparison of the observations with the $\mathcal{R} = 1$ model (dotted line) and the luminosity-dependent $N_{\rm H}$ distribution derived by Ueda et al. (2003, dashed line). All models are for the Ueda et al. (2003) XLF.

Also, this plot is constructed using the $N_{\rm H}$ probability density distribution for each source instead of the best-fitting solution. The advantage of this approach is that the column density uncertainties, due to small number of photons in the X-ray spectra, are taken into account in the analysis. Indeed, the C-statistic, used in the few counts limit, provides confidence limits and probability density distributions for the fitted parameters. In particular, the ΔC is distributed as χ^2 with ν degrees-of-freedom (where ν is the number of fitted parameters) and hence, the same methods used to estimate confidence intervals for the model parameters in the case of the χ^2 analysis also apply to the C-statistic for spectra with few counts (Cash 1979). We confirm this by performing simulations of power-law spectra with fixed $\Gamma = 1.8$ and different levels of X-ray obscuration. We verify that even to the limit of less than $\approx$10 photons the $N_{\rm H}$ probability density distribution estimated from the C-statistic is in agreement with that derived from the simulations.

Fig. 7 presents the predictions of the different $f(N_{\rm H})$ models discussed in the previous section combined with the Ueda et al. (2003) XLF. Comparison with the data suggests that the $\mathcal{R} = 2$ model is in broad agreement with the observations. The χ^2-test probability that the two distributions are drawn from the same parent population is about 51 per cent. Higher or lower values of $\mathcal{R}$ provide poorer fits and fail to predict the observed distribution. Using the χ^2 statistical test we estimate probabilities of 12 per cent for the $\mathcal{R} = 3$ model and $<$1 per cent for the $\mathcal{R} = 1$ and 4 models. For the Ueda et al. (2003) luminosity-dependent $f(N_{\rm H})$, we estimate a χ^2-test probability of about 71 per cent, somewhat better than the $\mathcal{R} = 2$ model, the best of the step function $N_{\rm H}$ distributions with fixed ratio $\mathcal{R}$. We note that the adopted XLF has little effect on the model $N_{\rm H}$ distributions shown in Fig. 7 and, therefore, does not alter our main conclusions.

We note, however, that our sample may comprise a number of Compton thick AGN ($N_{\rm H} > 10^{24}\,{\rm cm}^{-2}$) where the direct X-ray emission is completely blocked from view and the spectrum in the *Chandra* energy band is a pure reflection continuum. Fitting a single absorbed power law to these sources is clearly not appropriate and will produce erroneous $N_{\rm H}$ estimates. We attempt to quantify this effect by simulating reflection-dominated spectra and then fitting them with WABS*POW XSPEC models as described in Section 5. For this exercise we use the Compton reflection models of Magdziarz & Zdziarski (1995) as implemented in the PEXRAV SED of XSPEC. We assume a solid angle of 2π, solar abundance for all elements and an average inclination relative to the line of sight $\cos i = 0.45$. Only the reflection component was used, i.e. no direct radiation. We also add a Fe Ka iron line assuming a Gaussian profile with width $\sigma = 100$ eV, similar to the instrumental FWHM of the Advanced CCD Imaging Spectrometer (ACIS-I) and rest-frame equivalent width of 1 keV appropriate for heavily obscured AGNs ($N_{\rm H} > 10^{24}\,{\rm cm}^{-2}$; e.g. George & Fabian 1991). For the simulations we adopt a redshift $z = 1.5$ and fix the normalization so that the spectrum has a flux of about $5 \times 10^{-15}\,{\rm erg\,s^{-1}\,cm^{-2}}$ in the 2–10 keV band. The simulated spectra are fit with an absorbed power law as described in Section 5 to estimate the $N_{\rm H}$ our X-ray spectral analysis produces for this type of sources. The simulations give a narrow distribution for the estimated $N_{\rm H}$ in the range 10^{23}–$10^{24}\,{\rm cm}^{-2}$. We therefore underestimate the column density of these systems and it is likely that some of the sources in the range $N_{\rm H} \approx 10^{23} - 10^{24}\,{\rm cm}^{-2}$ in Fig. 7 should be moved to higher $N_{\rm H}$ values. We note, however, that even if some of the sources in this column density range are reflection-dominated Compton thick AGN, we do not expect this to modify our conclusions about the agreement between the data and different model $N_{\rm H}$ distributions. Unfortunately, the small number of counts in most of the obscured sources in our sample does not allow us to identify Compton thick AGN candidates dominated by reflection emission.

8 DISCUSSION

In this paper, we explore the redshift and the intrinsic $N_{\rm H}$ distributions of AGN using a deep 200-ks *Chandra* pointing in the GWS region. This is the first of a total of eight observations that are currently underway as part of a deep wide angle (0.5 deg^2) X-ray survey in the EGS. A wealth of optical photometric and spectroscopic data are available in this field (e.g. DEEP2, CFHTLS) providing optical identifications as well as spectroscopic and photometric redshift estimates for the X-ray population.

The advantage of this data set is that the detected sources are responsible for a sizable fraction of the XRB (about 70 per cent in the 2–10 keV band) and have mean X-ray spectral properties consistent with the XRB ($\Gamma \approx 1.4$; Nandra et al. 2005). Nevertheless they are, on average, brighter than the extremely faint X-ray population identified in the ultradeep *Chandra* surveys (Alexander et al. 2003) facilitating follow-up multiwavelength studies. For example, the hard X-ray selected sample comprises 97 sources of which 74 have $R < 24.5$ mag (76 per cent) and therefore are accessible for optical spectroscopy using 10-m class telescopes. For comparison, in the CDF-North a total of 332 sources are detected in the 2–8 keV spectral band of which 203 (60 per cent) have $R < 24.5$ mag and 162 (50 per cent) have optical spectroscopy available (Barger et al. 2003).

For comparison with the models we focus on the hard X-ray selected sample. This combines sufficient number of sources (97) for statistical reliability and high optical identification rate minimizing uncertainties due to optically faint X-ray sources. A total of 14 systems in this sample (14 per cent) are blank fields. Many of them also have $\log f_{\rm X}/f_{\rm opt} \gtrsim 1$. This is shown in Fig. 8 which plots $R_{\rm AB}$-band magnitude against 2–10 keV X-ray flux. High X-ray to optical flux ratio systems are suggested to comprise a large frac-

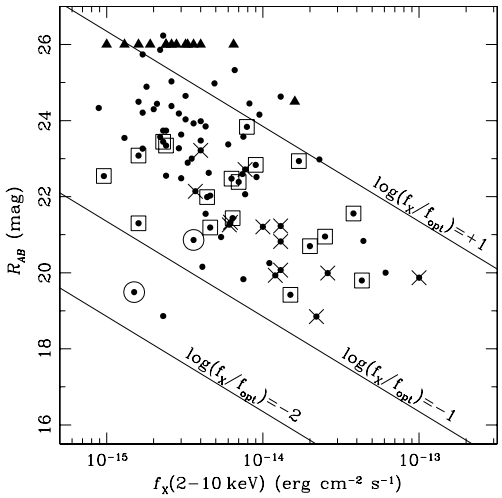

Figure 8. $R_{\rm AB}$-band magnitude against 2–10 keV flux for the hard-band selected sample. The lines $\log f_{\rm X}/f_{\rm opt} = \pm 1$ delineate the region of the parameter space occupied by powerful unobscured AGNs and are estimated from the relation $\log f_{\rm X}/f_{\rm opt} = \log f_{\rm X}(2\text{–}10\,{\rm keV}) + 0.4\,R_{\rm AB} + 5.46$. A cross on top of a symbol is for sources with broad-line optical spectra. Open squares and open circles on top of a dot correspond to sources with narrow emission line and absorption optical spectra, respectively. Triangles represent upper limits in optical magnitude for sources without optical identifications.

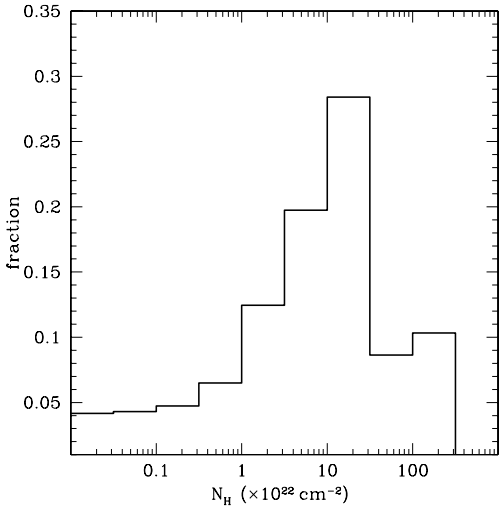

Figure 9. $N_{\rm H}$ distribution of the hard X-ray selected sources with no optical identification.

tion of high z heavily obscured type II QSOs (Mignoli et al. 2004; Civano, Comastri & Brusa 2005). Fig. 9 plots the $N_{\rm H}$ distribution of these sources assuming a mean redshift $z = 1.5$. The optically unidentified sources in the hard sample are skewed toward high column densities compared with identified sources, with a median of about $5 \times 10^{22}\,{\rm cm}^{-2}$.

The redshift distribution of the GWS hard-band sample, using both spectroscopic and photometric redshifts, shows a peak at $z \approx 1$. Although about 2/5 of the X-ray sources do not have redshift determination, we argue that these systems are unlikely to modify the shape of the $N(z)$. The observed redshift distribution in Fig. 6 is in agreement with previous deep surveys in the hard band that also find that the X-ray population peaks at $z \approx 1$ (Fiore et al. 2003; Georgantopoulos et al. 2004; Treister et al. 2004; Barger et al. 2005).

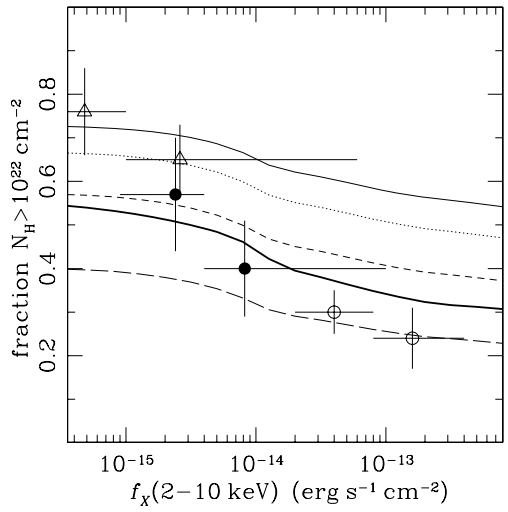

Figure 10. Fraction of sources with $N_{\rm H} > 10^{22}\,{\rm cm}^{-2}$ as a function of 2–10 keV flux. Open triangles: CDF-S adapted from Akylas et al. (2006); open circles: the *XMM–Newton* survey described by Akylas et al. (2006); filled circles: this study. The thin-line curves from bottom to top correspond to models with $\mathcal{R} = 1$–4. The bold curve is the model that uses the Ueda et al. (2003) $N_{\rm H}$ distribution.

This is at odds with the recent versions of the population synthesis models that successfully reproduce the spectral properties of the XRB but predict a peak at higher redshifts $z \approx 1.5$ (Comastri et al. 1995; Gilli et al. 2001). As demonstrated in Fig. 6, the origin of this discrepancy is that the models above adopt the XLF derived for soft band selected powerful QSO that peak at $z \approx 1.5$–2 (e.g Miyaji et al. 2000). More recent studies, however, that combine X-ray selected AGN samples over a wider luminosity range, suggest a more complex evolutionary history that strongly depends on $L_{\rm X}$: more powerful systems evolve up to $z \approx 2$ while less luminous sources peak at lower redshift, $z \approx 1$ (Ueda et al. 2003; Barger et al. 2005; Hasinger, Miyaji & Schmidt 2005). As shown in Fig. 6, such a luminosity-dependent density evolution can successfully reproduce the redshift distribution of our sample.

The above complex evolutionary pattern warrants some physical interpretation. It is possible that less luminous systems, suggested to comprise a higher fraction of type II AGN (Ueda et al. 2003; Barger et al. 2005; Akylas, Georgantopoulos & Georgakakis 2006), are linked to starburst activity with a peak at $z \approx 1$ (Ballantyne, Everett & Murray 2006), while more powerful sources follow the QSO evolution peaking at $z \approx 2$. In this direction, the large fraction of hard (5–10 keV) X-ray selected sources with mid-IR counterparts (Fadda et al. 2002) has motivated models where obscured X-ray sources are tied to the IR-luminous population with an evolution that steeply rises to $z \approx 1$ and levels off at higher z (Franceschini, Braito & Fadda 2002; Gandhi & Fabian 2003). These models produce a redshift distribution for the faint X-ray population with a peak at $z \approx 1$ and also provide acceptable fits to both the spectral shape of the XRB and the source counts. We note that a possible association of X-ray obscuration and star-formation activity has also been proposed to interpret the sub-mJy radio properties of X-ray selected AGNs (Bauer et al. 2002; Georgakakis et al. 2004). The models above, however, require revision of the basic assumption of the unification model that requires that types I and II sources evolve in lockstep, since they are drawn from the same parent population.

A key issue in the study of the origin of the XRB is the intrinsic $N_{\rm H}$ distribution of AGN. Even moderate amounts of gas ($N_{\rm H} \approx 10^{22}\,{\rm cm}^{-2}$) have a strong effect on the X-ray emission below about 2 keV and therefore this issue is better addressed by observations at harder energies. In this respect, X-ray surveys in the 2–10 keV band at relatively bright fluxes ($\gtrsim 10^{-14}\,{\rm erg\,s^{-1}\,cm^{-2}}$) suggest that the observed fraction of AGN with $N_{\rm H} > 10^{22}\,{\rm cm}^{-2}$ is inconsistent with the locally determined fraction of 4:1 (Maiolino & Rieke 1995) and closer to a ratio of about 1:1 (Fiore et al. 2003; Georgantopoulos et al. 2004; Perola et al. 2004; Akylas et al. 2006). Therefore, XRB models that adopt a fixed 4:1 fraction of obscured AGNs independent of redshift or luminosity have a problem reproducing the observations at bright fluxes (e.g. La Franca et al. 2005; Treister & Urry 2005; Akylas et al. 2006). Surprisingly, deeper X-ray surveys show a different picture, suggesting an abrupt increase of the fraction of obscured AGNs at faint fluxes ($\lesssim 10^{-15}\,{\rm erg\,s^{-1}\,cm^{-2}}$; Perola et al. 2004; Treister et al. 2004; Akylas et al. 2006). This is demonstrated in Fig. 10 plotting X-ray flux against fraction of AGN with $N_{\rm H} > 10^{22}\,{\rm cm}^{-2}$ for both the bright *XMM–Newton* survey of Akylas et al. (2006) and the CDF-S. We note that for the latter field the $N_{\rm H}$ of each source is estimated using spectral fitting instead of hardness ratio. A full description of the spectral analysis in the CDF-S is presented by Akylas et al. (2006). In the same figure, the results from the EGS survey, split into two independent flux bins, are in broad agreement with the Akylas et al. (2006) study within the uncertainties. Also plotted in this figure are the predictions of the different $f(N_{\rm H})$ models described in Section 6 adopting the Ueda et al. (2003) XLF. We note that the adopted XLF has little effect on the model curves plotted in Fig. 10. At bright fluxes the observations are in better agreement with $\mathcal{R} \approx 1$, while at fainter fluxes the data are progressively more consistent with higher $\mathcal{R}$ models. This may suggest a luminosity-dependent $N_{\rm H}$ distribution similar to that proposed by Ueda et al. (2003). This model is indeed in fair agreement with our data at intermediate fluxes but is not as successful at both the faint and the bright end of Fig. 10, although somewhat better than a simple fixed-$\mathcal{R}$ $N_{\rm H}$ distribution. This may suggest a steeper luminosity dependence of the obscured AGN fraction compared to the Ueda et al. (2003) parametrization: i.e. $\approx$0.8 at $L_{\rm X} \approx 10^{42}\,{\rm erg\,s^{-1}}$ decreasing to about 0.2 at $L_{\rm X} \approx 10^{45}\,{\rm erg\,s^{-1}}$ compared to $\approx$0.6 and 0.3, respectively, for the Ueda et al. (2003) model. We note that a number of recent studies, using ultradeep and/or shallow wide-angle samples, also argue in favour of a luminosity and/or redshift-dependent $N_{\rm H}$ distribution to explain the observed properties of the X-ray population (La Franca et al. 2005; Treister & Urry 2005; Akylas et al. 2006).

A luminosity-dependent fraction of obscured AGN can be understood in terms of modified unification schemes. In these models the inner radius and/or the geometric height of the torus vary with the power of the central engine because of dust evaporation and radiation pressure (e.g. Lawrence 1991; Simpson 2005).

9 CONCLUDING REMARKS

This paper presents first results from an ongoing deep (200 ks per pointing) X-ray *Chandra* survey in the EGS region. Data from the first of a total of eight pointings in this field are used here. We analyse and discuss the optical and X-ray properties of the sample in the context of XRB population synthesis models.

We first construct the photometric and spectroscopic redshift distribution of the 2–10 keV selected sample to the limit $\approx 8 \times 10^{-15}\,{\rm erg\,s^{-1}\,cm^{-2}}$ which has a peak at $z \approx 1$ in agreement with previous studies. Although there is about 40 per cent redshift incompleteness we find that luminosity-dependent density evolution, where lower luminosity systems peak at lower redshifts, is in fair agreement with the observations. Luminosity functions that assume evolution out to $z \approx 2$ for the entire AGN population (both types I and II), similar to that of unobscured broad-line QSOs do not fit the data. The luminosity-dependent evolution supported by our data is consistent with scenarios suggesting that lower-luminosity systems (dominated by obscured AGNs) are associated with star-formation activity and peak at $z \approx 1$, while more powerful QSOs evolve out to higher z.

We also explore the $N_{\rm H}$ distribution of the sample which is consistent with either a fixed obscured AGN fraction of $\mathcal{R} \approx 2$ or the luminosity-dependent $N_{\rm H}$ distribution proposed by Ueda et al. (2003), where less luminous systems comprise a higher fraction of type II AGNs. We also argue that such luminosity-dependent parametrization of the $N_{\rm H}$ distribution is essential to account for the fraction of obscured AGN observed in different samples over a wide range of flux limits.

The X-ray survey of the EGS region, when completed, will cover a total of about 0.5 deg^2 at flux limits similar to those presented here. The final sample will be about eight times larger, comprising a total of over 1000 sources. The wealth of follow-up optical photometric and spectroscopic data available in this field (DEEP2, CFHTLS) will provide optical identifications as well as spectroscopic and photometric redshift estimates for a large fraction of the X-ray population, for example close to 90 per cent for the hard band. The use of *Spitzer* mid-IR data will further increase the number of X-ray identifications and also has the potential to refine the photometric redshift estimates, particularly for the optically faint subsample. Such a high identification rate combined with photometric/spectroscopic redshifts and the complementary multiwavelength data (IR, radio, sub-mm) available for the EGS promise a major step forward in our understanding of the nature and the evolution of the AGN populations that make up the XRB.

ACKNOWLEDGMENTS

We thank the anonymous referee for valuable comments and suggestions. AG acknowledges funding from PPARC and the Marie-Curie Fellowship grant MEIF-CT-2005-025108. This work uses data obtained with support of the National Science Foundation grants AST 95-29028 and AST 00-71198. Funding for the DEEP2 survey has been provided by NSF grant AST-0071048 and AST-0071198. Some of the data presented herein were obtained at the W. M. Keck Observatory, which is operated as a scientific partnership among the California Institute of Technology, the University of California and the National Aeronautics and Space Administration. The Observatory was made possible by the generous financial support of the W. M. Keck Foundation. The DEEP2 team and Keck Observatory acknowledge the very significant cultural role and reverence that the summit of Mauna Kea has always had within the indigenous Hawaiian community and appreciate the opportunity to conduct observations from this mountain.

Based on observations obtained with MegaPrime/MegaCam, a joint project of CFHT and CEA/DAPNIA, at the CFHT which is operated by the National Research Council (NRC) of Canada, the Institut National des Sciences de l'Univers of the Centre National de la Recherche Scientifique (CNRS) of France and the University of Hawaii. This work is based in part on data products produced at the Canadian Astronomy Data Centre as part of the CFHTLS, a collaborative project of NRC and CNRS.

REFERENCES

Akylas A., Georgantopoulos I., Georgakakis A. 2006, A&A, in press (astro-ph/0606438)
Alexander D. M., Brandt W. N., Hornschemeier A. E., Garmire G. P., Schneider D. P., Bauer F. E., Griffiths R. E., 2001, AJ, 122, 2156
Alexander D. M. et al., 2003, AJ, 126, 539
Antonucci R., 1993, ARA&A, 31, 473
Babbedge T. S. R. et al., 2004, MNRAS, 353, 654
Ballantyne D. R., Everett J. E., Murray N., 2006, ApJ, 639, 740
Baldi A., Molendi S., Comastri A., Fiore F., Matt G., Vignali C., 2002, ApJ, 564, 190
Barger A. J. et al., 2003, AJ, 126, 632
Barger A. J., Cowie L. L., Mushotzky R. F., Yang Y., Wang W.-H., Steffen A. T., Capak P., 2005, AJ, 129, 57
Bauer F. E., Alexander D. M., Brandt W. N., Hornschemeier A. E., Vignali C., Garmire G. P., Schneider D. P., 2002, AJ, 124, 2351
Brandt W. N. et al., 2001, AJ, 122, 2810
Brinchmann J. et al., 1998, ApJ, 499, 112
Bruzual A. G., Charlot S., 1993, ApJ, 405, 538
Cash W., 1979, ApJ, 228, 939
Civano F., Comastri A., Brusa M., 2005, MNRAS, 358, 693
Coil A. L., Newman J. A., Kaiser N., Davis M., Ma C.-P., Kocevski D. D., Koo D. C., 2004, ApJ, 617, 765
Coleman G. D., Wu C.-C., Weedman D. W., 1980, ApJ, 43, 393
Comastri A., Setti G., Zamorani G., Hasinger G., 1995, A&A, 296, 1
Cooper M. C. et al., 2006, MNRAS, in press
Downes A. J. B., Peacock J. A., Savage A., Carrie D. R., 1986, MNRAS, 218, 31
Faber S. M. et al., 2005, ApJ, submitted (astro-ph/0506044)
Fadda D., Flores H., Hasinger G., Franceschini A., Altieri B., Cesarsky C. J., Elbaz D., Ferrando P., 2002, A&A, 383, 838
Fiore F. et al., 2003, A&A, 409, 79
Fomalont E. B., Windhorst R. A., Kristian J. A., Kellerman K. I., 1991, AJ, 102, 1258
Franceschini A., Braito V., Fadda D., 2002, MNRAS, 335, L51
Gambill J. K., Sambruna R. M., Chartas G., Cheung C. C., Maraschi L., Tavecchio F., Urry C. M., Pesce J. E., 2003, A&A, 401, 505
Gandhi P., Fabian A. C., 2003, MNRAS, 339, 1095
Gandhi P., Crawford C. S., Fabian A. C., Johnstone R. M., 2004, MNRAS, 348, 529
Georgakakis A., Hopkins A. M., Afonso J., Sullivan M., Mobasher B., Cram L. E., 2004, MNRAS, 354, 127
Georgakakis A., Georgantopoulos I., Akylas A., 2006, MNRAS, 366, 171
Georgantopoulos I., Georgakakis A., Akylas A., Stewart G. C., Giannakis O., Shanks T., Kitsionas S., 2004, MNRAS, 352, 91
George I. M., Fabian A. C., 1991, MNRAS, 249, 352
Giacconi R. et al., 2002, ApJS, 139, 369
Gilli R., Salvati M., Hasinger G., 2001, A&A, 366, 407
Groth E. J., Kristian J. A., Lynds R., O'Neil E. J., Jr, Balsano R., Rhodes J., 1994, AAS, 185, 5309
Gruber D. E., Matteson J. L., Peterson L. E., Jung G. V., 1999, ApJ, 520, 124
Gwyn S. D. J., 2001, PhD thesis, Univ. Victoria
Hasinger G., 2003, Nucl. Phys. B. Suppl. Ser. (astro-ph/0310804)
Hasinger G., Miyaji T., Schmidt M., 2005, A&A, 441, 417
Hopkins A. M., Connolly A. J., Szalay A. S., 2000, AJ, 120, 2843
Kim D.-W. et al., 2004, ApJS, 150, 19
Kinney A. L., Calzetti D., Bohlin R. C., McQuade K., Storchi-Bergmann T., Schmitt H. R., 1996, ApJ, 467, 38
Kitsionas S., Hatziminaoglou S., Georgakakis A., Georgantopoulos I., 2005, A&A, 434, 475
La Franca F. et al., 2005, ApJ, 635, 864
Lawrence A., 1991, MNRAS, 252, 586
Lehmer B. D. et al., 2005, ApJS, 161, 21
Lilly S. J., Le Fevre O., Crampton David H. F., Tresse L., 1995, ApJ, 455, 50
Magdziarz P., Zdziarski A. A., 1995, MNRAS, 273, 837
Maiolino R., Rieke G. H., 1995, ApJ, 454, 95
Mignoli M. et al., 2004, A&A, 418, 827
Miyaji T., Hasinger G., Schmidt M., 2000, A&A, 353, 25
Morrison R., McCammon D., 1983, ApJ, 270, 119
Nandra K., Pounds K. A., 1994, MNRAS, 268, 405
Nandra K. et al., 2005, MNRAS, 356, 568
Perola G. C. et al., 2004, A&A, 421, 491
Reeves J. N., Turner M. J. L., 2000, MNRAS, 316, 234
Risaliti G., Maiolino R., Salvati M., 1999, ApJ, 522, 157
Rosati P. et al., 2002, ApJ, 566, 667
Sarajedini V. et al. 2006, ApJ, in press (astro-ph/0605370)
Simpson C., 2005, MNRAS, 360, 565
Steidel C. C., Adelberger K. L., Shapley A. E., Pettini M., Dickinson M., Giavalisco M., 2003, ApJ, 592, 728
Steidel C. C., Shapley A. E., Pettini M., Adelberger K. L., Erb D. K., Reddy N. A., Hunt M. P., 2004, ApJ, 604, 534
Treister E., Urry M. C., 2005, ApJ, 630, 115
Treister E. et al., 2004, ApJ, 616, 123
Ueda Y., Akiyama M., Ohta K., Miyaji T., 2003, ApJ, 598, 886
Virani S. N., Treister E., Urry M. C., 2006, AJ, 131, 2373
Voght N. P. et al., 2005, ApJS, 159, 41
Webb T. M. A., Lilly S. J., Clements D. L., Eales S., Yun M., Brodwin M., Dunne L., Gear W. K., 2003, ApJ, 597, 680
Weiner B. J. et al., 2005, ApJ, 620, 595
Willmer C. N. A. et al., 2005, ApJ, submitted (astro-ph/0506041)
Wisotzki L., 1998, Astron. Nachr., 319, 257
York D. G. et al., 2000, AJ, 120, 1579

This paper has been typeset from a TEX/LATEX file prepared by the author.